12-2013

Interaction of Fast Highly Charged Ions with Insulating Straight and Tapered Glass Capillary Surfaces

Asmaa Mohammed Ayyad
Western Michigan University, asma.ayyad@wmich.edu

INTERACTION OF FAST HIGHLY CHARGED IONS WITH INSULATING STRAIGHT AND TAPERED GLASS CAPILLARY SURFACES

by

Asmaa Mohammed Ayyad

A dissertation submitted to the Graduate College
in partial fulfillment of the requirements
for the degree of Doctor of Philosophy
Physics
Western Michigan University
December 2013

Doctoral Committee:

John A. Tanis, Ph.D., Chair
Emanuel Y. Kamber, Ph.D.
Asghar N. Kayani, Ph.D.
Nikolaus Stolterfoht, Ph.D.

INTERACTION OF FAST HIGHLY CHARGED IONS WITH INSULATING STRAIGHT AND TAPERED GLASS CAPILLARY SURFACES

Asmaa Mohammed Ayyad, Ph.D.

Western Michigan University, 2013

Transmission of fast highly charged ions through insulating single straight cylindrically-shaped and tapered funnel-shaped glass capillaries of microscopic dimensions has been studied using MeV/u proton and oxygen beams. The beams, obtained from the WMU tandem Van de Graaff accelerator, were transmitted through the capillaries and then counted with a silicon surface barrier detector.

The interaction between 1 and 3 MeV protons and 12, 16 and 24 MeV O^{5+} ions and the inner walls of the straight and tapered glass capillaries was investigated by measuring the transmission energy dependence. The straight capillaries had diameters of 0.18 and 0.14 mm and lengths of 14.4 and 11.2 mm, respectively, for an aspect ratio of 80 for both samples. The tapered capillary had an inlet diameter of 0.71 mm, an outlet diameter of 0.1 mm and a length of 28 mm for an outlet to inlet area ratio of $20x10^{-3}$. The obtained data were reproducible for the energies used and the results indicate that the incident ions traverse the capillaries without significant energy loss. The transmission dependence on the incident charge state was examined using 16 MeV O^{5+} to O^{8+} ions on the tapered capillary. The results obtained show that the incident charge state has the

maximum transmission through both capillaries with the existence of small fractions of ions (< 1%) that capture an electron or lose one, two or three electrons.

ACKNOWLEDGMENTS

This research was done at Western Michigan University and it was not possible without help and support from many people in the physics department, family members and friends. This is a great opportunity to express my deep thanks and appreciation for everyone who offered time and advice to help me through my Ph. D. journey.

There are not enough words to express my gratitude and love to my parents for their infinite support, encouragement and prayers through all the past years without them I could not be at this level in my life. I would like to express my thanks and appreciations to my husband Mohammed Muhaisen and my sons Ameen, Imam and Ebaa Muhaisen for their sacrifice and patience, also to my sister Ms. Alaa Ayyad and my brother Mr. Mutaz Ayyad for their infinite support.

My great gratitude and thanks to my advisor Professor John A. Tanis who accepted me in his great group and supported me during this research with his guidance, advice and infinite patience. Without him this work would not be possible. I would also like to acknowledge him for the nice relationship he made with me and all the group members. He is not a physics advisor only, and we had a lot of gatherings with him that make me feel we are one family and he is always concerned about my life and my kids and always trying to help. I could not find enough words to thank him.

I would like also to give my special and deep thanks to Professor Asghar N. Kayani for his infinite help in the accelerator lab and for his courage and advice which definitely made this work successful. Also to Professor Emanuel Y. Kamber and Professor Nikolaus Stolterfoht, my committee members for reviewing this dissertation. Help and support from Rick Welch, Allan Kern and Benjamin Gaudio in preparations for the experiment are highly appreciated. My special thanks to my colleagues Dr. Buddhika S. Dassanayke, Dr. Susanta Das, Ms. Darshika Keerthisinghe, Dr. Elias J. Garratt, and Mr. Amila Dissanayake for their appreciated help in the lab work.

Last but not least my special thanks go to Prof. Dean Halderson, the graduate advisor, and Prof. Kirk Korista, the physics department chair, for their support and guidance. I thank the physics department for the infinite corporeal and incorporeal support. To everybody else who helped me along the way a big thank you.

"Oh Allah, Glory cry in which extended his hearty where peace and another cry that the praise be to Allah, the Lord of the Worlds"

Asmaa Mohammed Ayyad

TABLE OF CONTENTS

Table of Contents-Continued

CHAPTER

LIST OF TABLES

LIST OF FIGURES

List of Figures-Continued

List of Figures-Continued

List of Figures-Continued

CHAPTER I

INTRODUCTION

The interaction of highly charged ions (HCIs) with conducting (1,2) and insulating (3,4) surfaces took considerable attention in the last two decades to understand the transmission mechanisms as well as the uses in potential technological applications. The rapid growth of nanotechnology makes it possible to manufacture nano-sized capillaries as well as the micro-sized capillaries which are used in experiments in order to understand the HCI interactions with the inner wall of the capillaries that enable the production of micro- and nano-sized HCI beams that have a wide range of valuable applications (5, 6).

Since then several studies have been performed on metallic micro-capillary foils using slow HCIs. It was found that a large number of electrons are transferred from the target valance band into the excited outer most shells of the ion producing a stabilized hollow atom or hollow ion (7) that can pass through the capillary without suffering from close collisions with the capillary inner wall. The hollow atoms can be extracted in vacuum for relatively long lifetimes on the order of nanoseconds (8). These results have applications in beam capillary spectroscopy (9).

Slow HCIs were also used with insulating capillaries and the results showed guiding (3), i.e., first the ions hit the inner wall of the capillary and charged it positively, and then the following ions are deflected towards the capillary exit by the positive charge

build up on the inner surface. Most of the incident ions transmit through the capillary without any close collision with the inner surface (10). Moreover, the insulating capillaries were used to study the transmission of fast HCIs (11) and the obtained results showed that the transmitted beam density was higher compared to the incident beam density (the transmitted beam was enhanced) and no energy loss was found.

In this work the interaction of fast protons and oxygen ions through insulating microscopic dimension straight glass capillaries with diameters of 0.18 and 0.14 mm and lengths of 14.4 and 11.2 mm, respectively, with an aspect ratio of 80 was investigated. Also a tapered glass capillary with an inlet diameter of 0.71 mm, an outlet diameter of 0.1 mm and a length of 28 mm for an aspect ratio of ~70 and outlet to inlet area ratio of $20x10^{-3}$ was investigated using variable incident energies for protons and oxygen ions and variable incident charge states for the oxygen ions. The experimental work was performed at the Western Michigan University Van de Graaff accelerator laboratory.

In chapter II background studies including the interaction of HCI with insulating capillaries are summarized. Chapter III shows the experimental apparatus and the experimental techniques and chapter IV shows the results for the straight and tapered glass capillaries in detail.

CHAPTER II

INTERACTION OF HIGHLY CHARGED IONS WITH INSULATING CAPILLARIES

Any interaction between charged atoms and surfaces depends on the atom (ion) kinetic and potential energy since energy transfer to the electronic system in the target causes atomic ionization or electronic excitation (12). In the case of slow ions (total kinetic energies ~ keV) the interaction is limited to the few layers close to the surface (13) whereas in case of fast ions (total kinetic energies ~ MeV) the ions can penetrate deeper in the target causing energy loss (14) by the ions and extend the region of reaction.

Guiding Phenomenon

Interaction of slow highly charged ions (HCIs) of 3 keV Ne^{7+} ions with ~100 nm diameter capillaries etched in insulating polyethylene terephthalate (PET) was studied in 2002 by Stolterfoht and his group (3). The obtained results show that the transmitted ions traveled through the capillary without touching the inner surface even though the capillary was tilted by up to 20^{o} with respect to the incoming ion beam direction (3,15). Since then this result is known as the guiding effect, where initially part of the incident ions interact with the capillary inner wall creating charge patches and these patches produce an electric field that is strong enough to deflect the following ions toward the capillary exit (16,17,18,19). The created patches are stationary after equilibrium is reached as long as the HCI beam is bombarding the capillary, and also the last charge

patch is extended around the capillary circumference (20). The guided ions maintain their initial energy and charge state (3,21,22) as described in the following schematic diagram.

When the incident HCI beam enters the capillary the incident ions impact the surface and leave their charge at the inner wall. Then by tilting the capillary axis with respect to the incident beam charge patches are produced downstream of the entrance patch farther inside the capillary creating a repulsive electric field through the capillary including the exit region. Hence the following ions are guided and centered around the capillary axis towards the exit. In this case the guided transmitted ions keep their energy and incident charge state.

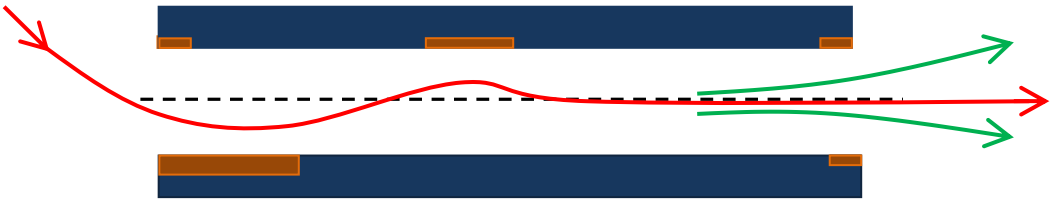

Figure 1. Slow HCI guiding scenario through an insulating capillary with colored solid lines representing the guided ions path, and small dark orange rectangles representing the charge patches (after Ref. 23) .

In order to understand the guiding mechanisms further different slow ion beams were used with different samples as shown in the following section.

Slow Ion Transmission

Slow ions having energies in the range of a keV were applied to study the guiding effect experimentally in nano- and micro-scale capillaries composed of different materials. The main key in ion guiding is the self-organizing process (24,10) where the incident ions create a charge patch (16,18) at the capillary entrance region by depositing their charge on the surface resulting in an electrostatic field. Building up of the charge patch is continued until it is sufficiently large to deflect the ions towards the capillary exit (25) after which the charge buildup at the entrance decreases to a rate just to keep the field. Later, while the ions traverse the capillary, temporary weaker charge patches are created inside that eliminate collisions with the inner wall, so the ions do not re-scatter from the capillary wall but are deflected and directed towards the exit (16,26) .

The exact number of charge patches depends on the material properties, the charge and the energy of the incident beam (16). Increasing the incident current (10) or the capillary density (27) does not change the charge patch at the entrance region. Increasing the incident energy of the ions reduces the width of the transmitted guided beam (21,28). On the other hand the guided beam keeps its initial charge state while guided through the capillary (29,30).

In subsequent experiments capillaries other than PET were used, i.e., highly ordered parallel SiO_2 nanocapillaries (20,31), polycarbonate nanocapillaries PC (32,33,34), and slow positive ions (35) through Al_2O_3 nanocapillary foils with the results

also proving the existence of the guiding effect. Negative ions with Al_2O_3 nanocapillary foils (36) were also investigated and the results show that the transmitted ions were neutralized or ionized into positive ions. Moreover, a single cylindrically-shaped glass of macro-sized capillary was used with slow ions and the results showed the guiding effect with the sample tilted up to 5^o with respect to the incident beam direction (37). Also, a dielectric (quartz) tube (38) and single tapered-shaped glass capillaries were used (39,40) showing that a slow ion beam can be guided by charge patches and the resulting electric field (41) and also the guided beam was focused due to the taper angle (42).

Electron Transmission

Transmission of electrons through nano- and-macro sized capillaries was investigated to compare the results with the slow ions for further understanding of interactions with insulating surfaces. Transmission of electron beams with incident energies between 200 and 350 eV through alumina nanocapillaries provided the first evidence of electron guiding through nanocapillaries (43).

Faster electron beams with incident energies of 500 and 1000 eV were used with polyethylene terephthalate nanocapillaries (PET), with the results also showing guiding but with significant energy loss (44) due to collisions with the inner walls of the capillaries pointing to inelastic scattering. Moreover, single straight glass macroscopic-sized capillaries, with electron energies between 1100 to 1500 eV (45) and 300 to 1000 eV (46) and a tapered glass capillary with energies 500 and 1000 eV (47) were used to

investigate the transmission and compare it with nano- and-micrometer sized foils. The results showed that the transmitted electrons suffer a significant energy loss (46) like the PET foils (44), and the tapered capillary showed guiding for the high energies and less transmission for lower energies (47).

The main reason behind the energy loss is the interaction with the capillary inner wall. Figure 2 explains the electron interactions with the capillary wall, where incident electrons are repelled by the Coulomb forces from existing charge patches as for slow ions (18) and transmitted through the capillary towards the exit. Higher energy electrons might interact with the capillary inner wall then be scattered from atoms near the surface and then transmitted through with energy loss or penetrate deeper into the bulk material and then be either transmitted through the capillary with a larger energy loss or be lost into the bulk of the capillary (48).

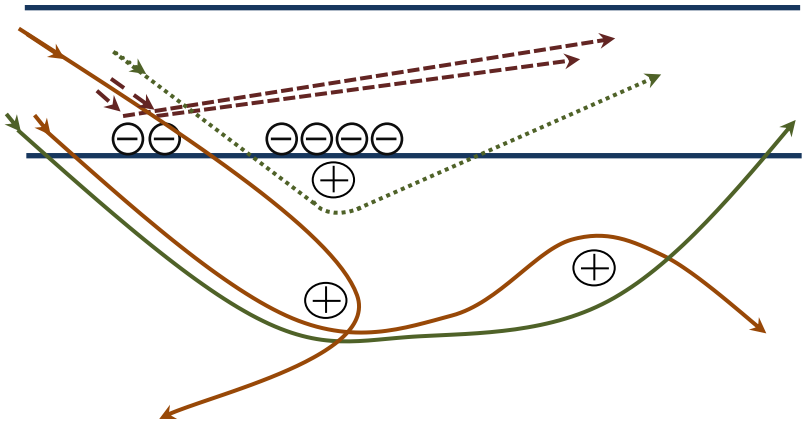

Figure 2. Electron transmission scenarios through a straight capillary. The dashed lines represent the path of Coulomb scattered electrons from surface charge build up, the dotted line represents the path of scattered electrons from atoms close to the capillary surface, and the solid lines represent the paths of electrons penetrating deeper into the bulk of the capillary and losing energy followed by either transmission (green line) or loss (brown line) into the bulk (after Ref. 48)

Transmission Factor

Fast Ions

Experimental studies including the interaction of fast HCIs with insulating surfaces were conducted in parallel with studies for slow HCIs. In 2003 Nebiki and his group injected 2 MeV He^+ ions into a single tapered glass capillary with an inlet diameter of 0.8 mm, outlet diameter of 0.3 μm and a length of 50 mm (11). The idea behind using the tapered capillary with fast ions followed that of a glass polycapillary bundle that was successfully used to enhance x-ray microbeams (49). The tapered capillary is a single glass tube that gets narrower towards the outlet; more details about fabrication can be

found on page 24 in this thesis. The experimental results showed that the transmitted ions did not lose energy and the transmitted beam density was enhanced compared to the incident beam density.

Several experiments took place to better understand the focusing effect using mostly single glass capillaries. The experimental results showed that most of the transmitted ions kept their kinetic energy (42,50,51,52,53) and incident charge states (54,55, 56) before and after the capillary was tilted with respect to the incident beam direction. There was no delay in the transmission unlike the slow ions as a sign of no charge build up being required for the ions in order to traverse the capillary without energy loss.

Hence the fast HCI transmission scenario through tapered capillaries could be explained as follows: the injected ions are transmitted through the capillary in a path parallel to the axis without interaction with the inner wall keeping their energy and charge state. Some ions do hit the inner wall near the exit due to the fact that the outlet is smaller than the inlet and bent towards the exit with a slight loss in energy. Moreover, some ions interact with the inner wall before the curvature inside the capillary (shown in figure 9) and suffer from multiple small angle scattering in different positions before they are able to exit the capillary with higher energy loss.

The transmission factor (sometimes referred to as the enhancement or focusing factor) is defined as the ratio of the transmitted current density to the incident current density. Hence the inlet and the outlet diameters of the tapered capillaries are the main

keys in determining the transmission of charged ion beams. The transmission effect in the tapered capillary is mainly due to the small-angle scattering from the capillary glass surface layer, since the capillary inner shape determines the escape probability of the scattered ions from the wall (51,57). The materials used to fabricate the capillary have an influence on the focused beam, e.g., lead glass can transmit the beam with slightly higher probability compared to borosilicate glass, but the transmission ratio was enhanced by a factor of two when the taper angle was constant throughout the capillary, i.e, conically-shaped capillary (58). On the other hand it was found that the transmission factor is current independent (51).

Slow Ions and Muons

The tapered glass capillaries were also used in applications to produce micro- and nano-meter sized beams of keV even though the transport mechanism of the fast ions is different. In the slow ions case, first the incident ions charge the front entrance of the capillary as explained earlier. The created additional charge patches in a self-organized charge up procedure farther along inside the capillary direct the ions towards the exit. Then the following ions are guided through the capillary keeping their incident kinetic energy and charge state (40). The capillary outlet is smaller than the inlet hence the transmitted ion beam density is enhanced with an output size similar to the capillary outlet inner diameter depending on the capillary taper angle (40,59).

Muons are used to study the magnetic properties of various materials like chemical compounds and biological samples due to their interaction with the local magnetic field of the samples. The obtained beams by the conventional methods (accelerator facilities) are relatively large for that purpose. Hence tapered glass capillaries were applied to enhance positive and negative muon beams in atmosphere. It was found that the enhancement factor could be higher if the tapered material is heavier (42,60). On the other hand, a straight glass capillary was used to adjust the direction of a slow ion beam mechanically (56) indicating that the need for the traditional optical tools, i.e., electric or magnetic deflection to position and adjust the beam direction for applications is minimized.

Applications

A transmitted micro- or nanometer sized ion beam has been used to analyze microsized areas of materials surfaces. The tapered glass capillary has been used as a compact, inexpensive and an easy-to-use device beside having the advantage of producing the needed output to focus slow and fast ion beams by the conventional methods.

Tapered glass capillaries are considered as a tool to enable surgery in an arbitrary region of any cell. The target can be determined very precisely by using a microscope after the beam energy is tuned, so that the deposition length along the beam direction is well defined. Then the desired beam (high energy) is injected into the target without air

between the beam and the cell (5,42). Beside cell surgery tapered glass capillaries were used to focus fast ions used in bacterial physiology (61). Moreover tapered glass capillaries were used in nuclear reaction analysis in producing high energy beams with a spot size on the order of μm (62).

CHAPTER III

EXPERIMENTAL TECHNIQUE

To study the interaction between fast highly charged ions (HCIs) and insulating glass macrocapillaries high energy beams of 1 and 3 MeV protons and 12, 16 and 24 MeV O^{5+} to O^{8+} were used. The beams used in the experimental work were obtained from the Western Michigan University (WMU) tandem Van de Graaff Accelerator.

In this chapter the beam production, experimental set up and the sample preparation are described.

WMU Accelerator

The tandem Van de Graaff accelerator shown in figure 3 has two main sources to produce negative ions, an Alphatross source and the source of negative ions by cesium sputtering (SNICS). The Alphatross source makes it possible to produce negative ions from gases, mainly He. This source is reliable and it has a long operational time (~ 1600 hours) before maintenance is required. The SNICS source produces negative ions from solids, and is also a reliable source and with longer operational times (~two years) in the absence of any accident. The negative ion beam from either source is attracted to the positive terminal of the accelerator where electrons are stripped by either a carbon foil or oxygen gas (used more often). More details about beam production are in the next

section. In this work the SNICS source was used to produce the proton and oxygen beams

There are four different beam lines at the facility, looking downstream from left to right in the schematic: the electron spectrometer chamber beam line at 30^{o} L, a surface analysis chamber at 0^{o}, a recoil ion chamber at 15^{o} R and a scattering chamber at 30^{o} R. The electron spectrometer chamber was the experimental chamber for the present work.

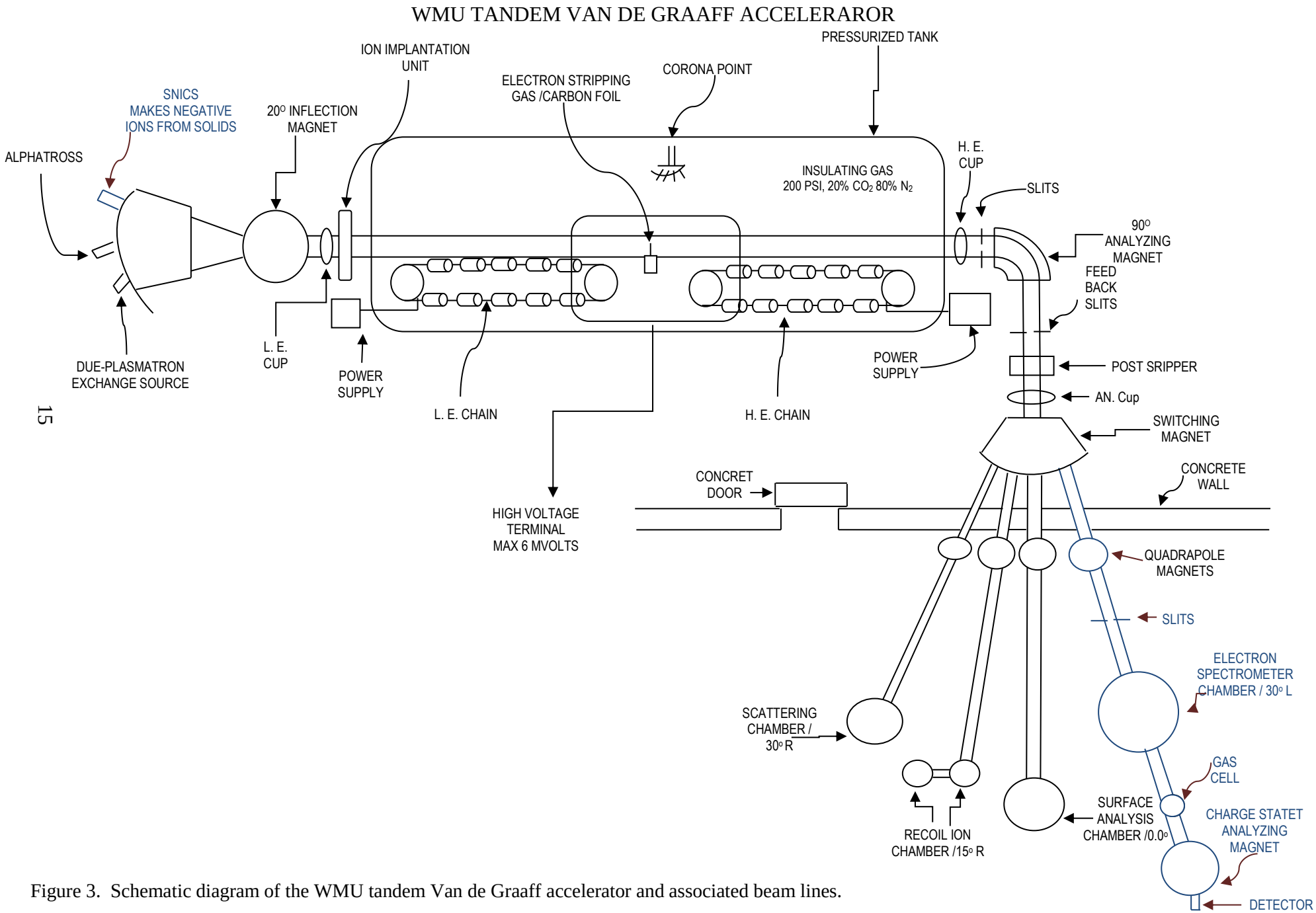

Figure 3. Schematic diagram of the WMU tandem Van de Graaff accelerator and associated beam lines.

Beam Production

The beam was obtained using the SNICS source by heating the cesium metal in the oven to ~ 160^{o} C following which cesium vapor rises in the vacuum into an enclosed area between the cooled cathode and the heated ionizing surface as shown in figure 4. Some of the cesium atoms are ionized by contact with the hot conical ionizer, while other cesium atoms are attracted to the sputtering cathode which was packed with (TiH_2) to produce protons or (Al_2O_3) to produce oxygen. The cathode was held at -6 kV with respect to the ionizer. The energetic cesium ions sputter atoms from the surface of the cathode and these atoms collide with the cesium atoms near the cathode and capture an electron and then become negative ions. Negative ions are repelled by the cathode and accelerated towards an extractor electrode which was at +13 kV and subsequently towards a final focus electrode.

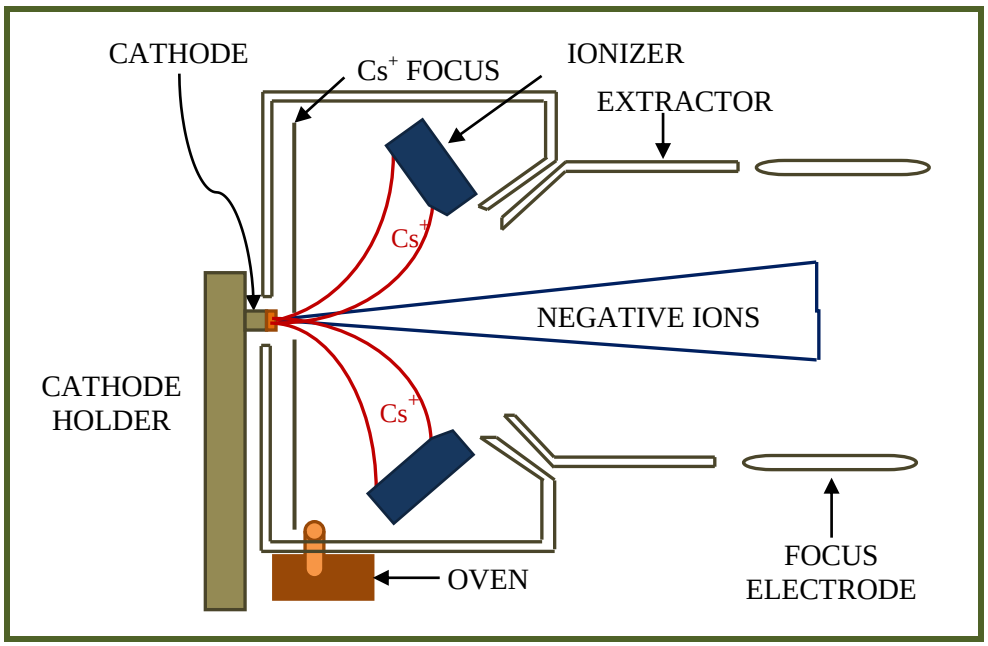

Figure 4. Schematic diagram of the SNICS source.

The obtained negative beam was analyzed by a 20^o inflection magnet, and then injected into the low energy side of the accelerator tube shown in figure 3. Voltages up to about 5.5 MV (V_t) can be maintained on the terminal located halfway along the inside of the accelerator tube. The negative ions were stripped at the terminal to become positive ions using either a gas stripper (used in this work) or a carbon foil located in the center of the tube and then accelerated to an energy of $E = (q+1)\ V_t$, where q is the charge of the positive ion. The ions were focused onto a set of slits upstream from the 90^o analyzing magnet. The produced ion beam consists of several charge states of different energies which were analyzed by the 90^o analyzing magnet in order to select the desired energy and charge state. The analyzing magnet bends the beam and forms an image at the second set of slits.

The current produced by the beam striking the feedback slits just downstream from the 90^o analyzing magnet was converted into a signal that was sent to the corona system in order to stabilize the terminal voltage. Then a switching magnet was used to select the proper beam line (30^o L in this work) in the target room.

The desired beam was focused by a quadrupole lens on the 30^o L line just past the switching magnet in the target room by monitoring the beam current on a four-jaw slit assembly located upstream of the experimental chamber as shown in figure 3 and 5, and on a collimator inside the experimental chamber upstream of the sample as shown in figure 5. The current on the sample was in the range 1 to 10 pA.

Experimental Setup

The desired beam entered the experimental chamber which was at a vacuum of ~10^{-6} Torr and struck the sample through a collimator of ~0.15 cm diameter located ~9 cm upstream of the sample as shown in figure 5. The sample was mounted onto an aluminum holder which was placed on a goniometer. The goniometer has two degrees of rotational freedom for precise positioning: one was rotation about the vertical axis (ψ) from -20^o to +20^o, and the other was azimuthal rotation about the horizontal axis from 0^o to 360^o with respect to the incident ion beam. The goniometer rotation can be controlled manually or automatically by LabView software.

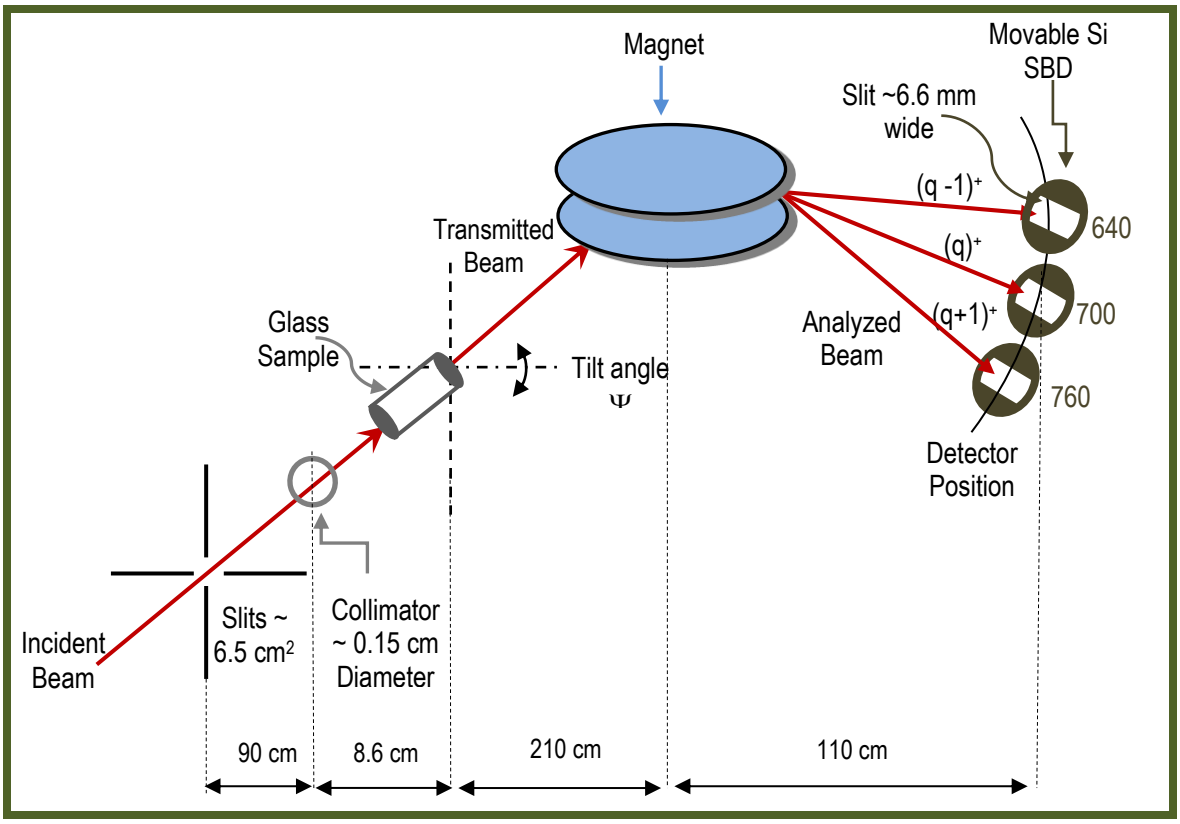

Figure 5. Schematic diagram of the experimental setup.

Rotation about the horizontal axis was used for alignment purposes only. Here, a TV monitor was held by the goniometer manual control showing the sample position on the telescope using a camera mounted on the telescope, and the sample was rotated around the horizontal and vertical axes manually to find the best aligned position with respect to the incident beam direction, which was then fixed as the zero position. The measured zero was not the same for each data set due to alignment. Rotation about the vertical axis only was used in collecting data and it was controlled automatically by the LabView software.

The transmitted ions were analyzed by a magnet located ~2 m downstream from the sample. The strength of the field in the magnet was changed according to equation 1 depending on the energy and charge state of the incident beam.

$$B_N = B_O \left(q_O / q_N\right) \sqrt{\frac{M_N E_N}{M_O E_O}} \qquad 1$$

B_N: the new magnetic field.	B_O: the previous magnetic field.
q_N: the new charge state	q_O: the previous charge state
M_N: the new mass	M_O: the previous mass
E_N: the new incident energy	E_O: the previous energy

Table 1. Equation 1 parameters

The analyzed beam was detected ~1 m downstream from the magnet by a movable silicon surface barrier particle detector (SBD) with a vertical aluminum slit ~ 0.7 cm wide installed onto the front of it. The detector could be moved manually around

the magnet in a circular path, starting from the zero position (at ~380 units) where a neutral ion can be detected and up to ~1000 units depending on how many charge states are expected. However it was found that 100 units in detector position are equal to a rotation of about 3^o or a displacement of ~3.3 cm. Table 2 shows the equivalent angles in degrees and distance in centimeters to the detector position units.

Detector Position (arb. units)	Angle θ (degrees)	Distance (cm)
380	0.0	0.0
400	0.6	0.7
500	3.6	4.0
600	6.6	7.3
700	9.6	10.6
800	12.6	13.8
900	15.6	17.1

Table 2. Detector position units converted to angles (deg) and displacement (cm).

In the case of O^{5+} ions, the incident charge state 5^+ was set to appear at detector position 700 according to the magnetic field applied using equation 1, while the lower (4^+) and the higher (6^+) charge states were detected about 60 units from the main charge state (5^+). This means that 4^+ appears at ~640 units or about 1.8^o from the 5^+ position and 6^+ appears at ~760 units, again about 1.8^o from the 5^+ position, and so on. Figure 6 shows plots of the charge state distributions for 1 MeV protons and 16 MeV O^{5+} versus the detector position at sample tilt angles $\psi = -0.6^o$ and $+0.3^o$ (measured zero) for protons and oxygen ions, respectively. The H^+ peak and O^{5+} peak, which are the main incident charge states, appear where the magnet was set for the peaks to be at detector position

700 and the other charge states for the oxygen beam appear where they are expected to be, i.e., 4^+ is at 635, 6^+ at 760, 7^+ at 825, and 8^+ at 890.

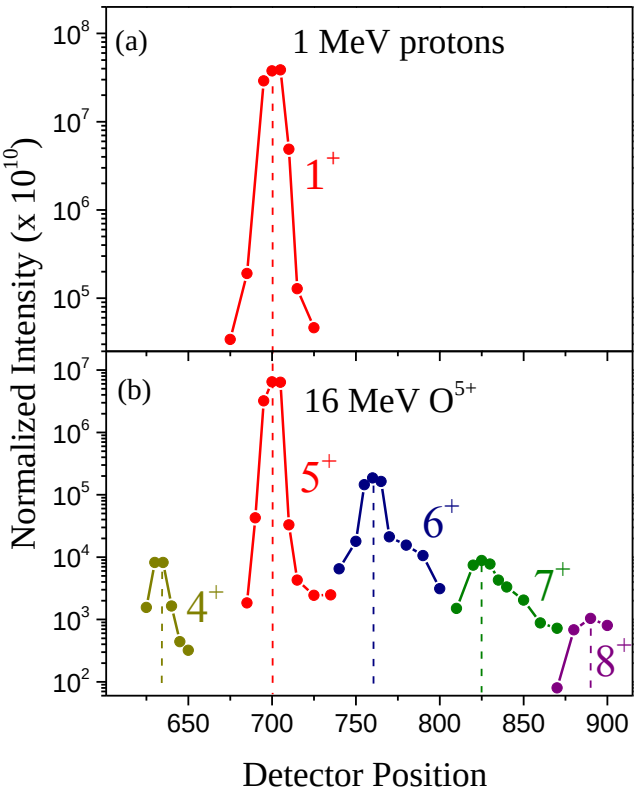

Figure 6. Normalized intensity to the incident current on the sample of the transmitted ions as a function of detector position for (a) 1 MeV protons and (b) 16 MeV O^{5+} ions.

A block diagram of the electronics used in the experiment is shown in Figure 7. The output signals from the silicon surface barrier detector were first input to a preamplifier (ORTEC 109A) and then input to the amplifier (TC 244). The bipolar signal was input to the oscilloscope to monitor the peak width and height, and to the counter. The unipolar signal was input to a multi-channel analyzer (MCA) and then sorted into a spectrum of number of counts versus the channel number. The current on the sample was read by a programmable electrometer (Keithley 617) with an output signal depending on the intensity of the sample current, and which gives a maximum 2V

DC output signal for full scale. This voltage output was dropped across a 1 MΩ resister to convert the voltage into a current. The current was then converted to logic pulses using a digital current integrator (DCI, ORTEC 439).

The MCA was used in the coincidence mode receiving a logic signal from the TIMER/COUNTER and the voltage signal from the amplifier to collect spectra for a certain number of counts for each detector position and for each tilt angle. The samples and the holder were coated with a conducting material to enable reading the current. The transmitted intensities were normalized to the current incident on the sample according to the formula in equation 2.

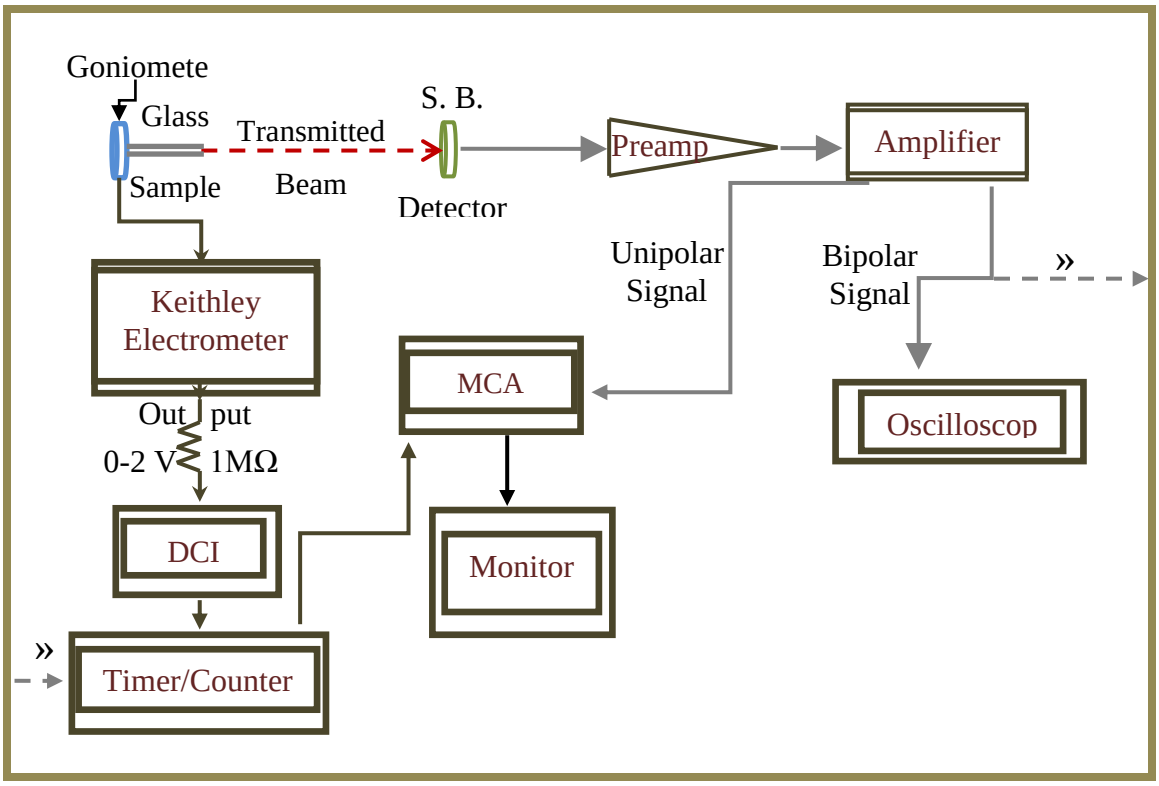

Figure 7. Schematic block diagram of the electronics

$$\text{Normalization Factor} = \frac{\text{(Number of counts)x (DCI scale) x(Keithley scale)}}{\text{(incident charge)x (e) x (Current)}} \qquad 2$$

The normalized intensities that appear on the computer monitor as peaks represent certain energies and figure 8 shows the energies used as a function of channel number with the red line indicating the linear fit results. Then using the straight line formula the energy for each spectrum was converted into channel number. Table 3 shows the converted values for the energies used.

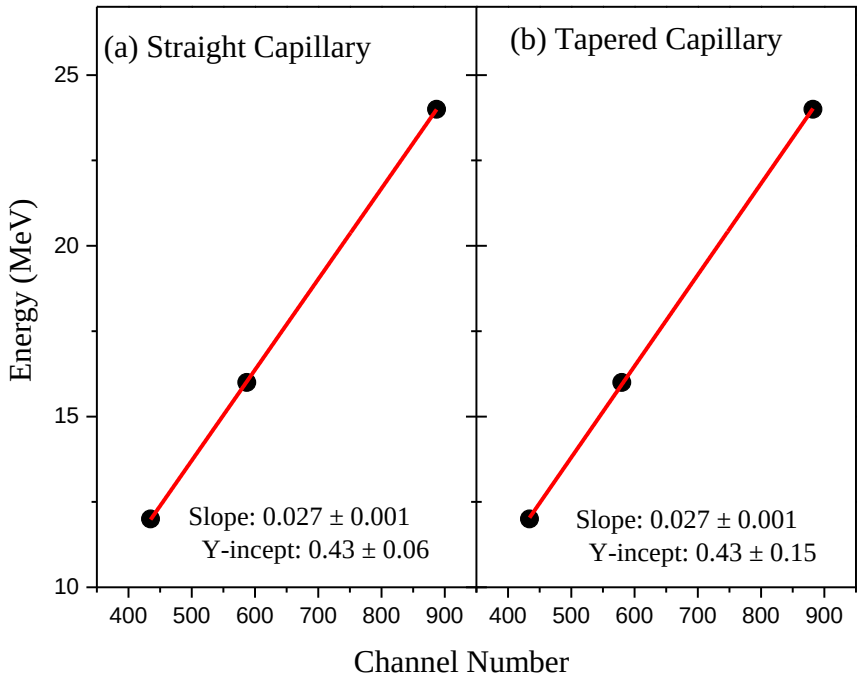

Figure 8. Energy as a function of channel number for: (a) the straight capillary and (b) the tapered capillary with the red line indicating the results of a linear fit.

Capillary	Energy (MeV)	Channel Number
Straight	12	435 ± 1
	16	585 ± 1
	24	886 ± 1
Tapered	12	433 ± 1
	16	586 ± 1
	24	883 ± 1

Table 3. The incident energies converted to channel number

Sample Preparation

Borosilicate is a type of glass for which the constituents are silica and boron dioxide ~ (80.6%) SiO_2, (13.0%) B_2O_3, (4.0%) Na_2O and (2.3 %) Al_2O_3 with a density of ~2.23 gm/cm^3. Borosilicate glass has a low thermal expansion and a softening temperature ~821^o C, making it a good candidate for studying the interactions of the fast HCIs with the samples where it cannot be melted or damaged easily due to the relatively low intensity of the beam. In this work single macroscopic-size borosilicate glass capillaries of straight and tapered shapes were used. A photograph of the capillaries is shown in figure 9.

The first sample was a straight glass capillary shown in figure 9a. Two straight glass capillaries were used: Capillary I, which had an inner diameter d of ~0.18 mm, and a length *l* of ~14.4 mm, and Capillary II, having an inner diameter d of ~0.14 mm and a length *l* of ~11.2 mm. Both samples have the same aspect ratio *l*/d ~80. The straight glass samples were prepared at the Institute of Nuclear Research of the Hungarian Academy of Sciences (ATOMKI), Debrecen, Hungary by Dr. Reka Béreczky. The

sample was made by heating a straight glass tube of ~1 cm diameter and stretching it with a constant force at the two ends. A special diamond cutter was used to cut the capillary in order to get the desired length. The inner diameter was measured using an optical microscope. The sample was fixed into an aluminum disk holder perpendicular to the capillary and then both the sample and the holder were covered with a thin layer of graphite to carry away the excess charges deposited on them and to prevent the build-up of charge on the sample (37).

The second sample was a tapered glass capillary shown in figure 9b, having an inlet diameter of ~0.71 mm, an outlet diameter of ~0.1 mm and a length of ~28 mm with an aspect ratio of 70 and an outlet to inlet area ratio of ~20 $x10^{-3}$. It was prepared at the RIKEN laboratory in Japan by Dr. Tokihiro Ikeda. The sample was made with the same procedure as the straight sample except that the tapered angle was controlled by tuning the temperature and the force (11, 39). The capillary was fixed perpendicular into an aluminum holder and coated using a thin layer of conducting silver paint.

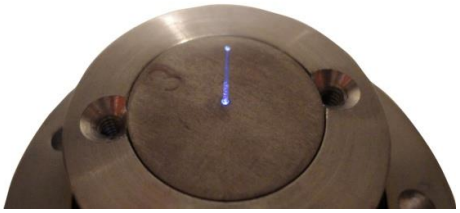

(a) Straight Glass Capillary

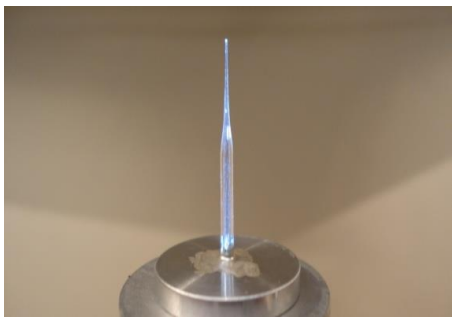

(b) Tapered Glass Capillary

Figure 9. Pictures of the samples for (a) the straight and (b) the tapered glass capillaries.

CHAPTER IV

INTERACTION OF FAST PROTONS AND OXYGEN IONS WITH GLASS CAPILLARIES

The interaction between HCIs and insulating solid surfaces was investigated intensively experimentally (3,10,11,15-16,18-23,27-48-50-59) and theoretically (4,17,24-26) in the last decade. The motivation was to understand the fundamental transmission mechanisms and to study the several applications as mentioned in chapter II.

In this chapter the transmission of 1 and 3 MeV protons and 12, 16 and 24 MeV O^{q+} ions through cylindrical and tapered shaped single glass capillaries of macroscopic dimensions is discussed. A collimated beam of ~1.5 mm diameter obtained from the WMU tandem Van de Graaff accelerator struck the front surface of the capillaries, which were coated with a thin layer of graphite for the straight capillary and silver for the tapered capillary. These coatings enabled reading the current on the sample and carrying away the excess charges deposited on them. The transmitted ions were analyzed by a dipole magnet located downstream from the capillary outlet to separate the emerging charge states as shown in figure 5. Following that, a silicon surface-barrier particle detector was used to count the transmitted ions to measure the intensities versus the magnetically analyzed position. The spectrum recorded at each detector position was normalized to the incident current on the sample according to equation 2. The transmitted intensities were measured for different incident tilt angles relative to the incident beam.

Proton Transmission through Straight and Tapered Capillaries

The transmission of 1 and 3 MeV protons through single straight glass capillaries of 0.18 and 0.14 mm diameter with an aspect ratio of 80 was investigated as a function of detector position and tilt angle. Also a tapered glass capillary with an inlet diameter of ~0.71 mm, an outlet diameter of ~0.1 mm and a length of ~28 mm with an aspect ratio of ~70 was investigated to understand the transmission mechanisms and compare with the straight capillary.

Transmission through the Straight Capillaries

The results for 1 and 3 MeV protons are shown in figure 10 where the y-axis represents the actual counts and the x-axis represents the energy in MeV. The energy values were obtained by converting the channel numbers in the actual spectra into energy according to the peak position assuming that the incident beam did not lose energy at detector position 700.

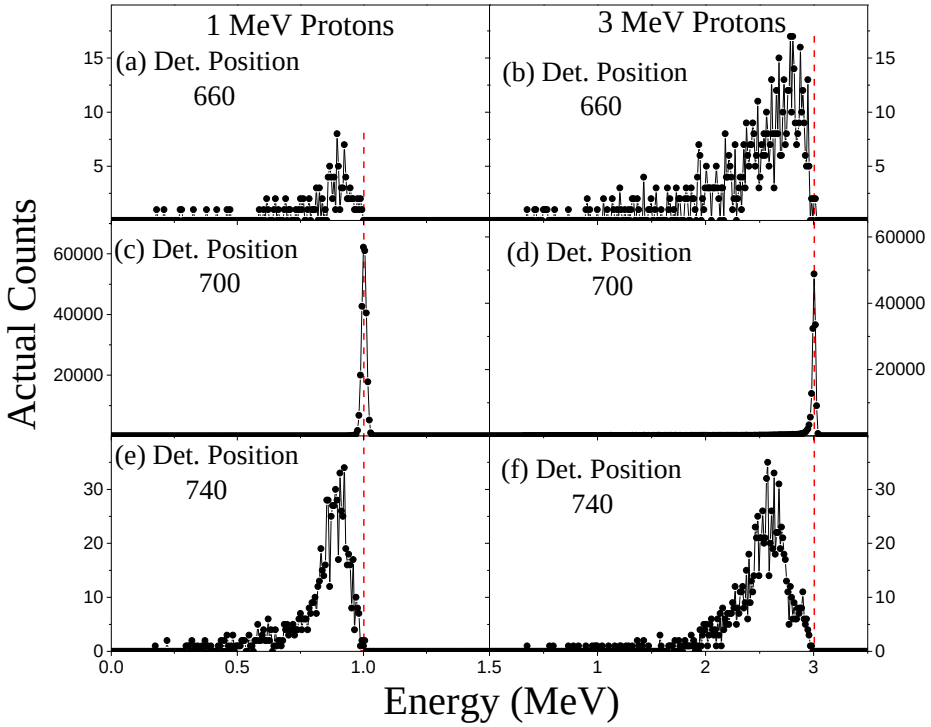

Figure 10. Spectra for 1 and 3 MeV protons at tilt angles of ψ = -0.9^o and -0.6^o, respectively, the measured zero angles for each energy, showing the peaks at detector positions: (a) and (b) 660, (c) and (d) 700, and (e) and (f) 740, with the dashed red line drawn at the incident energy.

Panels (c) and (d) in figure 10 show a sharp peak at detector position 700, where the main incident energy and charge state was set according to equation 2 (the detector position 700 is equivalent to $\theta \approx 9.6$ in degrees and a displacement of ≈ 10.6 in cm as shown in table 2). The sharp peaks represent the transmitted ions through the capillary which were assumed to occur without energy loss. Panels (a) and (b) show scattered ions at the detector position 660 ($\theta \approx 8.4^o$) before the main peak, and panels (e) and (f) show a peak at position 740 ($\theta \approx 10.8^o$) after the main peak, where drops in the number of counts by more than three orders of magnitude occur compared to the number of counts in panels (c) and (d). Also, the peaks in panels (e) and (f) are shifted to the left, indicating that the transmitted ions lost $\approx$ 0.11 MeV (~ 11%) in panel (e) and $\approx$ 0.42 MeV (~14%) in

panel (f) while traversing the capillary due to scattering from the capillary edges. Table 4 shows the centroid and the full width half maximum (FWHM) values for each peak.

Energy	Detector Position	Centroid (MeV)	FWHM (MeV)
1 MeV	660	0.90 ± 0.01	0.12 ± 0.01
	700	1.00	0.02 ± 0.01
	740	0.89 ± 0.01	0.13 ± 0.01
3 MeV	660	2.69 ± 0.01	0.55 ± 0.01
	700	3.00	0.03 ± 0.01
	740	2.58 ± 0.01	0.45 ± 0.01

Table 4. The centroid and FWHM values for the proton beam through the straight capillary.

Capillary I which had an inner diameter of 0.18 mm and a length of 14.4 mm was used first with 3 MeV protons, and capillary II with a diameter of 0.14 mm and a length of 11.2 mm was later used with the same beam energy and a new detector. The transmitted spectra for 3 MeV protons for capillaries I and II are shown in figure 11. The maximum intensity appears at detector position 700 as expected for both capillaries. However, the intensity falls off giving fewer counts as the tilt angle increases or decrease beyond the measured zero at $\psi = 0.4^{o}$ on both sides of the peak for capillary I and at $\psi = -0.6^{o}$ for capillary II. Both capillaries have the same aspect ratio as mentioned earlier and the transmission width in the figure is about 1^{o} and the drop in intensity is about two orders of magnitude for both capillaries as seen in panels (a) and (b).

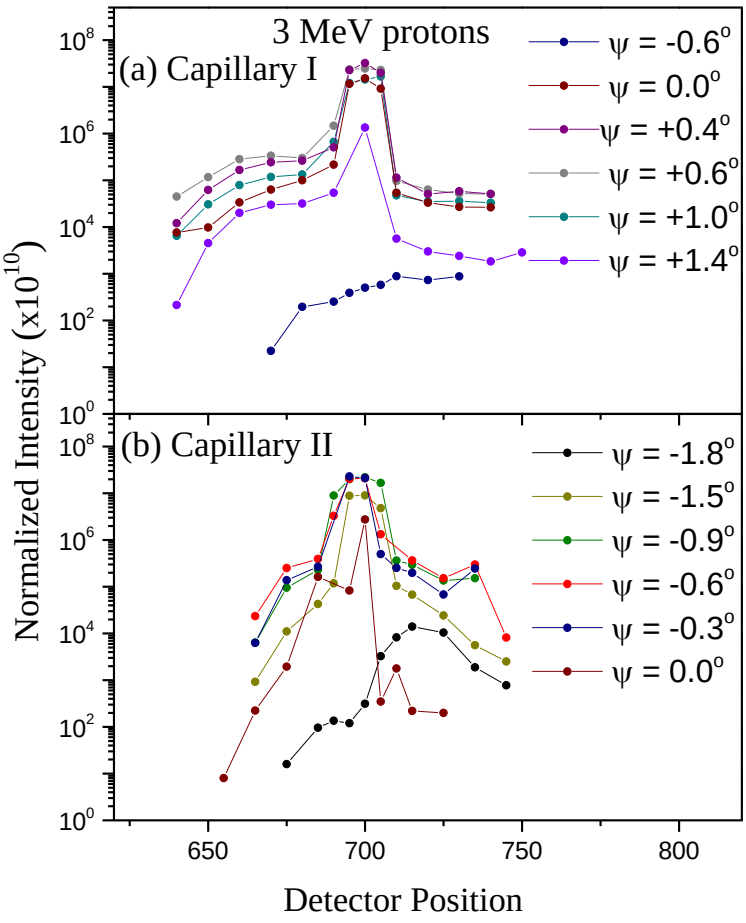

Figure 11. Normalized intensity of the transmitted ions as a function of detector position for 3 MeV protons at several tilt angles for (a) capillary I and (b) capillary II.

The peaks shown in figure 11 were integrated then plotted as a function of tilt angle as shown in figure 12. Panel (a) shows the spectrum for capillary I and panel (b) shows the spectrum for capillary II. Fitting a symmetric Gaussian to the data (solid red line) gives the FWHM values of each curve; these values are similar within the uncertainties as seen in the figure and the maximum intensity is ~4 x10^8 for both capillaries.

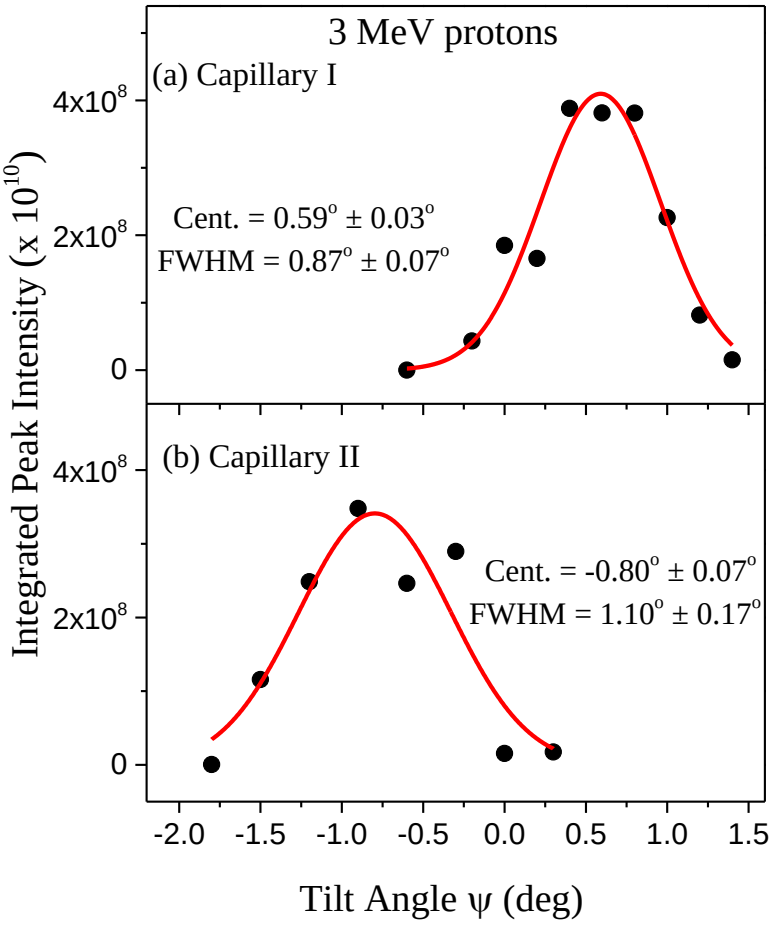

Figure 12. Integrated peak intensity as a function of tilt angle ψ (deg) for 3 MeV protons, with the solid red line indicating the results of a Gaussian fit for (a) capillary I and (b) capillary II.

The centroid values have different values since the data were taken at different times and with slightly different but unintentional alignments. The results shown in figures 11 and 12 indicate that the data are reproducible using two samples with the same aspect ratio.

Capillary II was used to investigate the transmission of 1 MeV protons to compare the results with the 3 MeV protons. The normalized intensities of the

transmitted protons versus the detector position are shown in panel (a) of figure 13 along with the results for 3 MeV from Fig. 11 shown in panel (b).

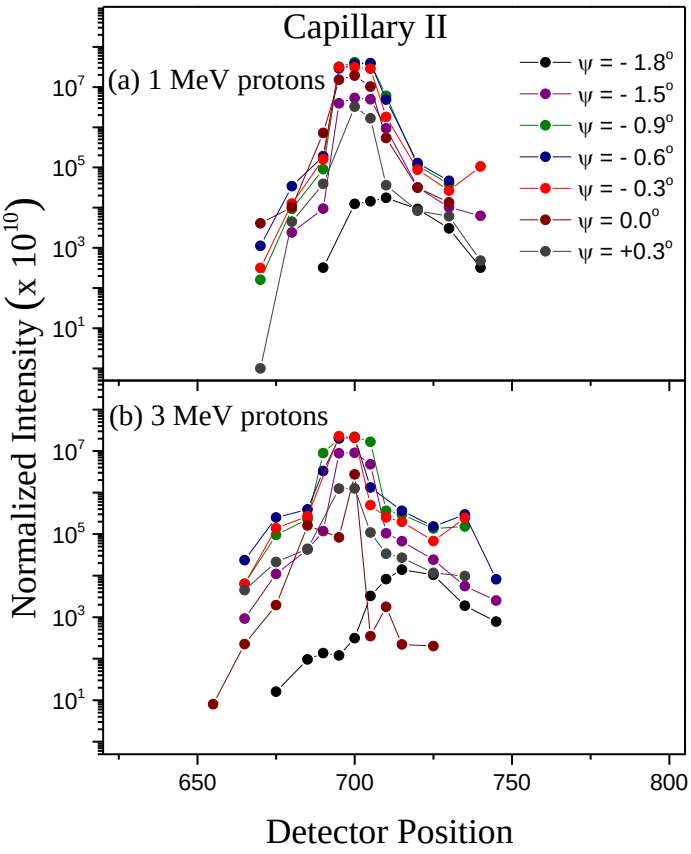

Figure 13. Normalized intensity of the transmitted ions as a function of the detector position on capillary II at several tilt angles: (a) 1 and (b) 3 MeV protons.

The maximum intensity is ~4 x10^7 for 1 MeV shown in the upper panel and ~2 x10^7 for 3 MeV shown in the lower panel, appearing at ψ = -0.6^o (measured zero) and detector position 700 in both cases. Tilting the sample between -1.5^o and 0.0^o indicates that the intensity falls off on both sides as the tilt angle goes away from ψ = -0.6^o by at least two orders of magnitude for both incident energies. Figure 14 shows the integrated

peak intensities as a function of tilt angle. Fitting a symmetric Gaussian to the data (solid red line) gives the FWHMs which are the same within the uncertainties.

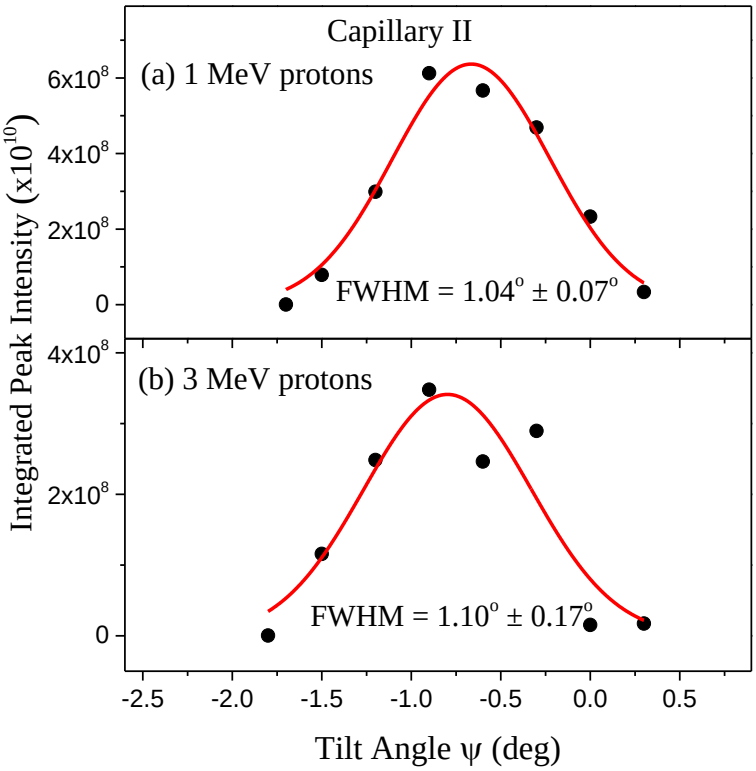

Figure 14. Integrated peak intensity for capillary II for (a) 1 and (b) 3 MeV protons, with the solid red line indicating the results of a Gaussian fit.

Transmission through the Tapered Capillary

As mentioned earlier the same setup and energies were used with the tapered capillary to compare the protons transmission through the two different capillaries. Figure 15 shows the actual number of counts versus energy in a similar way as shown in figure 10. Panels (c) and (d) show a sharp peak at detector position 700 ($\theta \approx 9.6^{o}$) which represents the transmitted ions through the tapered capillary without energy loss. The peak in panel (c) for 1 MeV shows fewer counts by a factor of three compared to the peak

in panel (d) for 3 MeV. Panel (a) shows scattered ions shifted to the left at the detector position 680 ($\theta \approx 9.0^o$) just before the main peak with a few counts compared to panel (c), while panel (b) at the same position ($\theta \approx 9.0^o$) shows a peak shifted to the left with two orders of magnitude fewer counts compared to panel (d). Panels (e) and (f) show a peak at position 730 ($\theta \approx 10.5^o$) after the main peak also shifted to the left indicating that the transmitted ions lost energy while traversing the capillary due to scattering from the capillary edges and the number of counts drops off by less than three orders of magnitude.

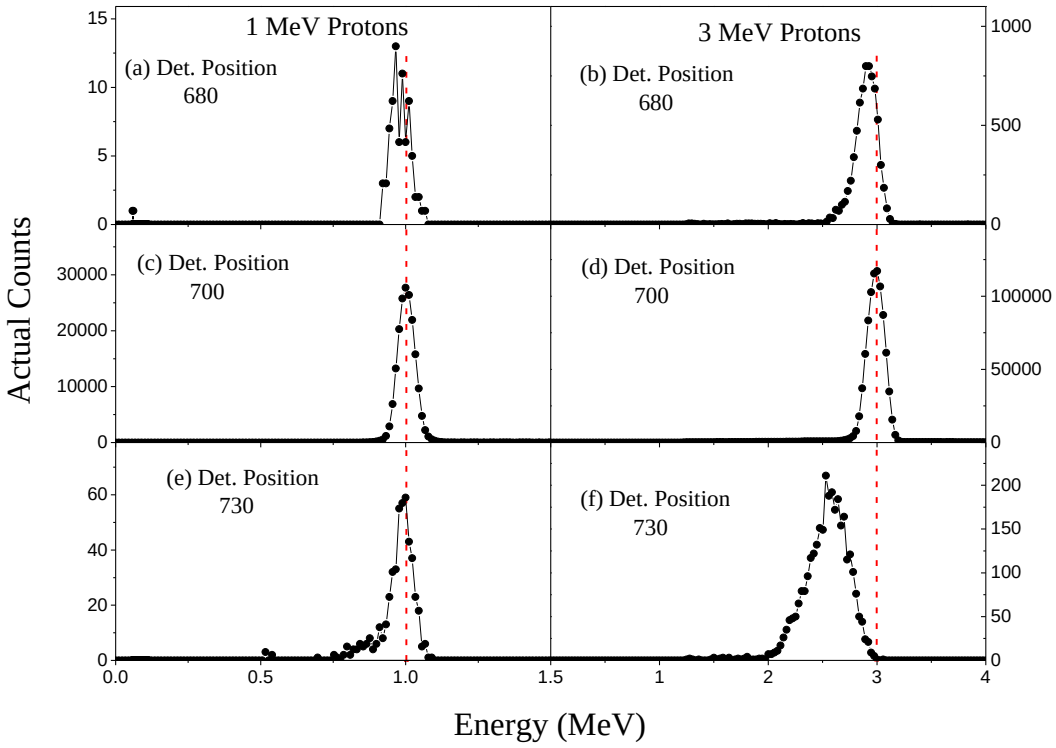

Figure 15. Spectra for 1 and 3 MeV protons at tilt angles of $\psi = +0.7^o$ and $+0.6^o$, the measured zero angles, respectively, showing the peak at detector positions: (a) and (b) 680, (c) and (d) 700, and (e) and (f) 730, with a dashed red line drawn at the incident energy.

The peak shown in panel (e) is slightly shifted to the left by about 0.1 MeV or 1% indicating that the transmitted ions traverse the capillary without a significant energy loss and the peak in panel (f) is shifted to the left by about ~0.44 MeV or ~15%. The centroid and the FWHM values of the peaks in figure 15 are given in table 5. The centroid values show that the transmitted protons for 1 MeV lost 2% and the 3 MeV lost 3% of their incident energy at detector position 680, and less energy loss for 1 MeV ~1% at detector position 730 while the 3 MeV lost ~15% of its energy. On the other hand the peak width is the same within the uncertainties for 1 MeV, while the values are not the same within the uncertainties for the 3 MeV as shown in table 5.

Energy	Detector Position	Centroid (MeV)	FWHM (MeV)
1 MeV	680	0.98 ± 0.01	0.08 ± 0.01
	700	1.00	0.07 ± 0.01
	730	1.00 ± 0.01	0.08 ± 0.01
3 MeV	680	2.91 ± 0.01	0.22 ± 0.01
	700	3.00	0.19 ± 0.01
	730	2.56 ± 0.01	0.43 ± 0.01

Table 5. The centroid and FWHM values for the proton beam through the tapered capillary.

Figure 16 shows the transmitted protons at several tilt angles versus the detector position for both energies. The maximum intensity is ~1 x10^7 for 1 and 3 MeV as shown in panel (a) and (b), respectively. Tilting the capillary between 0.0^o and $+0.9^o$ indicates

that the intensity falls off on both sides of the peak as the tilt angle goes away from ψ = +0.7° (measured zero) by three orders of magnitude for 1 MeV as shown in panel (a). Tilting the capillary between -0.3° and +0.9° indicates that the intensity falls off on both sides as the tilt angle goes away from ψ = +0.6° (measured zero) by at least two orders of magnitude for 3 MeV as shown in panel (b).

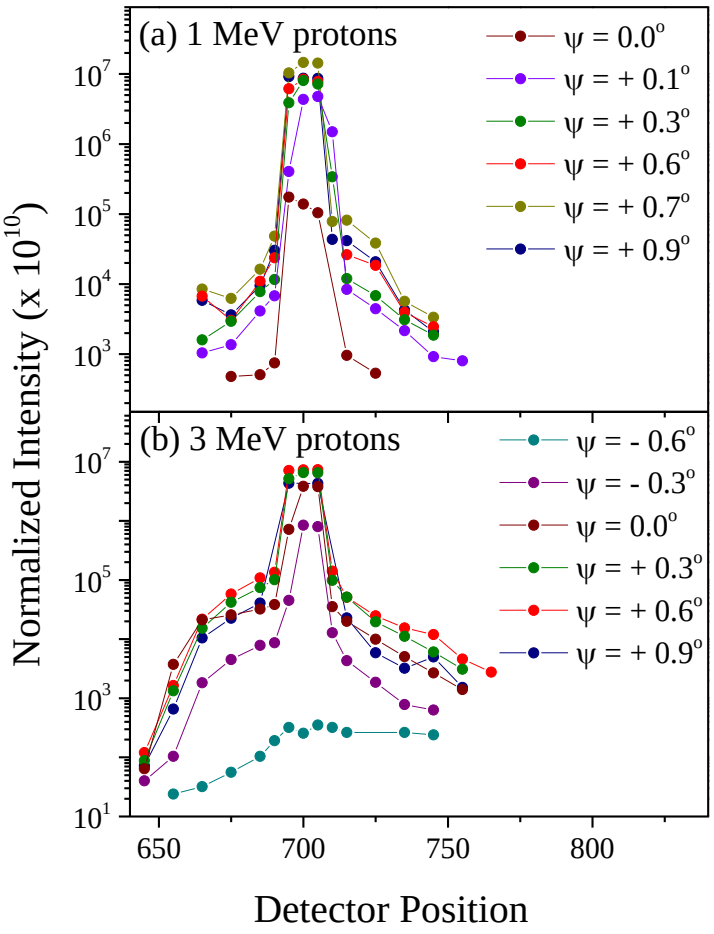

Figure 16. Normalized intensity of the transmitted ions as a function of detector position for the tapered capillary at several tilt angles for: (a) 1 and (b) 3 MeV protons.

The FWHM values in detector position units for each peak shown in figure 16 for the tapered capillary along with the results from figure 13 for the straight capillary as a

function of tilt angle are shown in figure 17. The FWHM values for both capillaries and both energies are about 13.4 units in detector position which is about 0.4° and 0.44 cm.

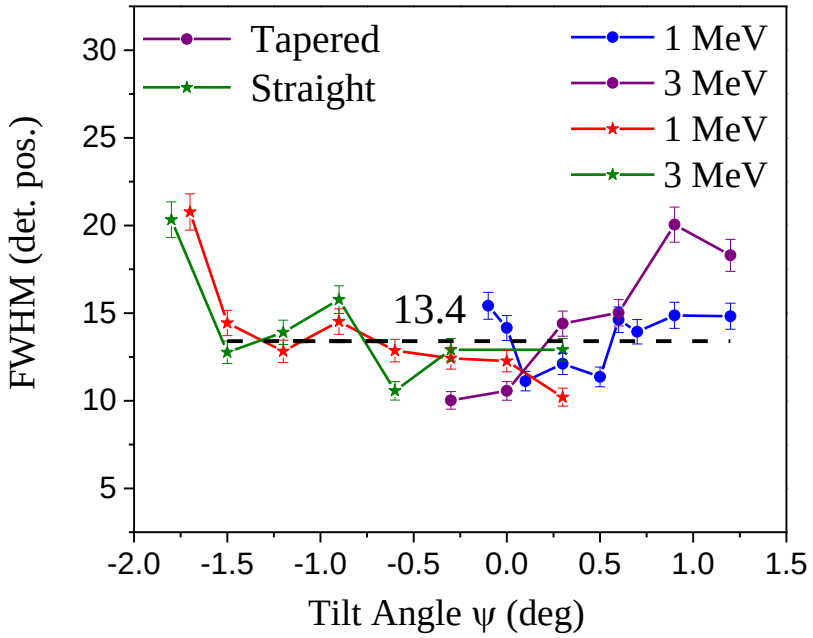

Figure 17. The FWHM values with error bars in detector position units for the straight and tapered capillaries for 1 and 3 MeV protons as a function of tilt angle ψ in degrees, with the dashed black line indicating the results of a linear fit.

Figure 18 shows the integrated peak intensities as a function of tilt angle for 1 and 3 MeV protons for the tapered capillary along with the results for 1 and 3 MeV protons for the straight capillary from Figure 14. Panels (a) and (c) show the results for 1 MeV on the straight and the tapered capillary, respectively, and panels (b) and (d) shows the results for 3 MeV also for the straight and the tapered capillaries, respectively. The FWHM values are the same within uncertainties for the tapered capillary for the energies used; also they are the same for the straight capillary at the energies used with the tapered capillary having a narrower width due to the different shapes of the capillaries. There is a drop in intensity by a factor of two between the different energies for the same capillary

as shown in panels (a) and (b) for the straight and panels (c) and (d) for the tapered capillaries indicating that with lower energy the higher the transmission. Also the straight capillary has about four times more intensity than the tapered capillary for the same energies probably due to the capillary size and shape.

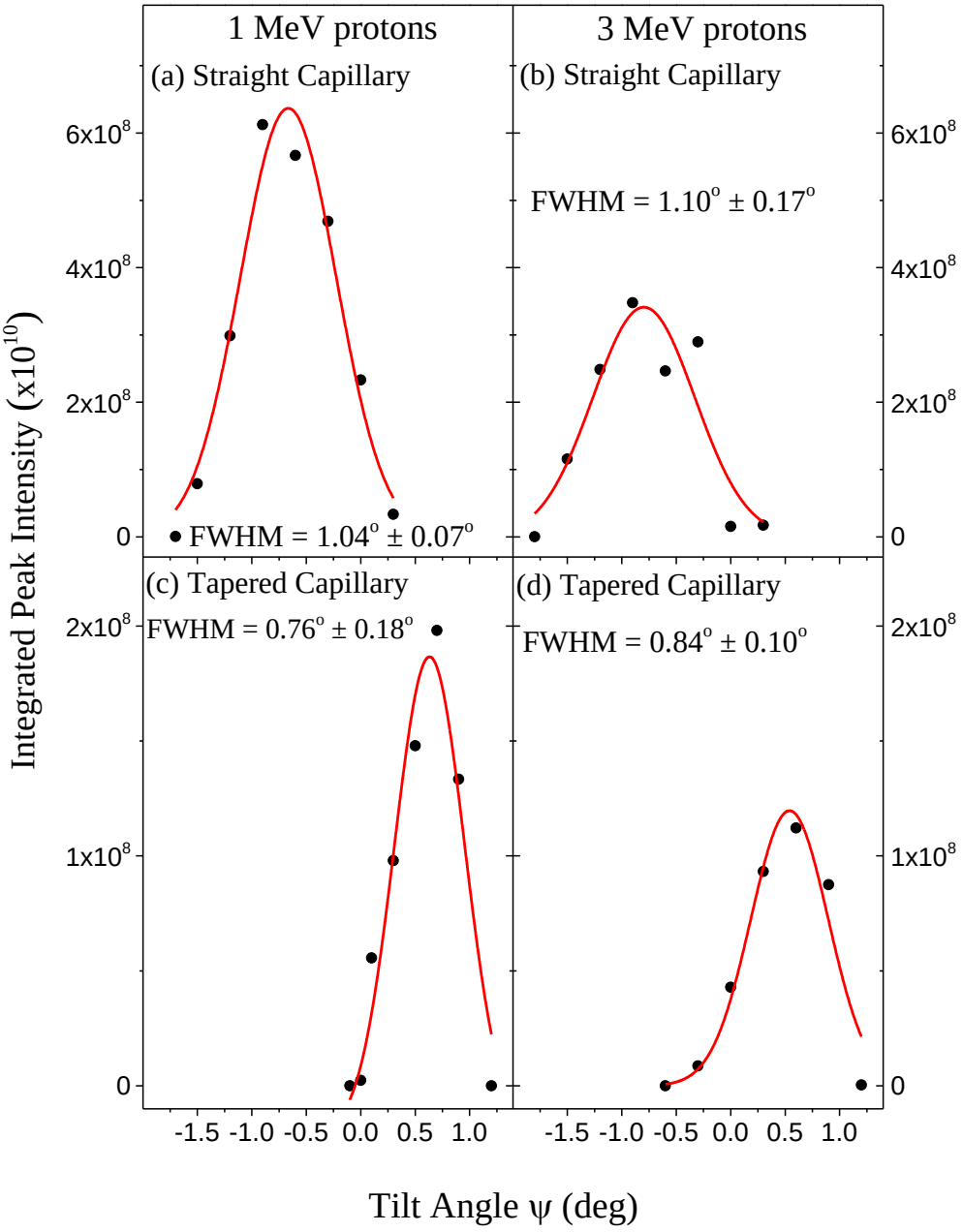

Figure 18. The integrated peak intensity for the straight and the tapered capillaries at (a) and (c) 1 MeV and (b) and (d) 3 MeV protons, respectively, as a function of tilt angle ψ (deg), with the solid red line indicating the results of a Gaussian fit.

Oxygen Transmission through Straight and Tapered Capillaries

The transmission of oxygen ion through the straight capillaries which have an aspect ratio of 80 and the tapered capillary that has an aspect ratio of 70 was investigated to study the dependence of energy and charge state and to compare the results with the hydrogen in order to better understand the transmission mechanisms. The proton (H^+) has no electron so it is structureless, while the oxygen (O^{5+}) has two electrons in the K shell and one in the L shell, which makes it structured compared to the proton. For these purposes three different beam energies for oxygen ions were used, specifically, 12 (0.75 MeV/u), 16 (1 MeV/u) and 24 (1.5 MeV/u) MeV with the straight and the tapered capillaries keeping the incident charge state (5+) fixed. Then the incident energy was fixed at 16 MeV (1 MeV/u) and the incident charge state was varied (5+, 6+, 7+ and 8+) with the tapered capillary only.

Transmission through Straight Capillaries

Straight capillary II was used to investigate the transmission of 12, 16 and 24 MeV O^{5+} starting with 16 MeV O^{5+} (1 MeV/u) to compare the results with 1 MeV protons for better understanding of the transmission mechanisms. Figure 19 shows the actual counts for 16 MeV O^{5+} ions on capillary II as a function of the detected energy, with the channel number being converted into energy as described earlier in chapter III. Panel (b) shows a sharp symmetric peak for 5+ with the maximum number of counts at detector position 700 ($\approx 9.6^o$), which represents the primary incident energy and charge state. Panel (a) shows a peak representing the captured ions 4+ at detector position 635

(≈8.7°) having about the same energy with three orders of magnitude fewer counts compared to panel (b).

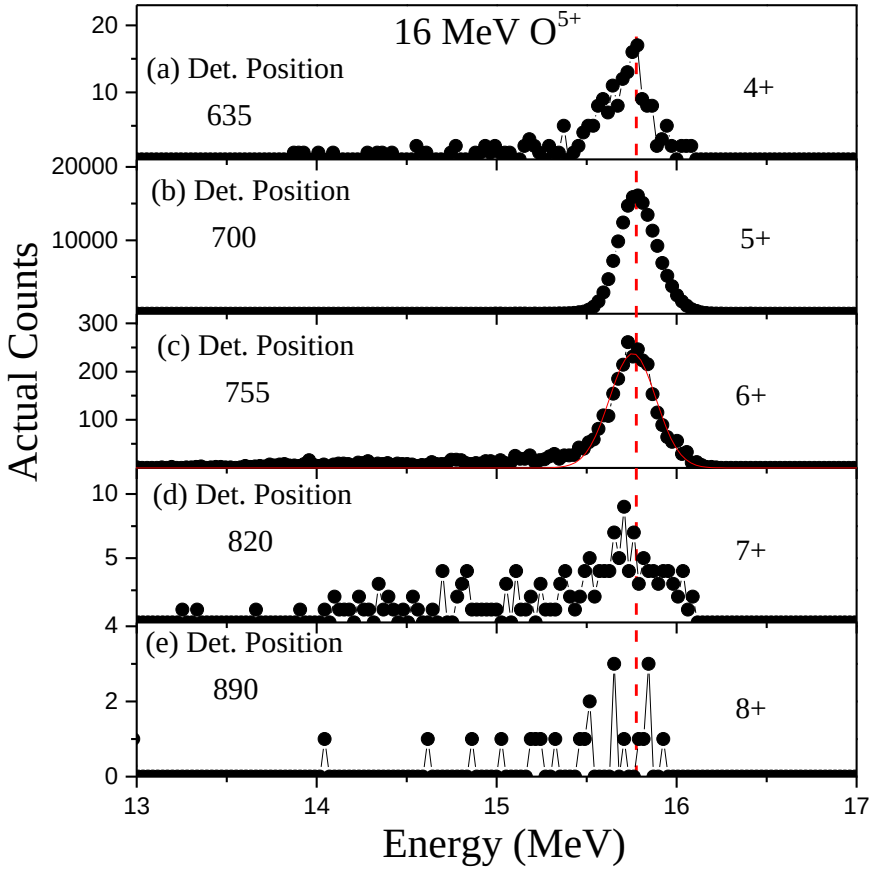

Figure 19. Spectra for 16 MeV O^{5+} ions at tilt angle ψ = +0.3° (measured zero) showing the peak at detector position (a) 635 for 4+, (b) 700 for 5+, (c) 755 for 6+, (d) 820 for 7+, and (e) 890 for 8+, with the dashed red line drawn at center of the main peak.

In panel (c) 6+ appears at detector position 755 (≈ 11.3°) showing an asymmetric peak with the number of counts dropping down by about two orders of magnitude compared to panel (b). Moving the detector farther, another peak comes at the position 820 (≈13.3°) as shown in panel (d). This peak represents 7+ with more than three orders of magnitude fewer counts compared to 5+. Moving the detector even farther shows

scattered counts appearing at the detector position 890 (≈15.3^{o}) as shown in panel (e) representing 8+.

Figure 20 shows the actual counts for 12 MeV O^{5+} as a function of the detected energy obtained by converting the channel numbers into energy as mentioned in chapter III. Panel (b) shows the sharp symmetric peak that represents the primary incident energy and charge state. Panel (a) shows a peak representing the captured 4+ ions having about the same energy as 5+ with more than two orders of magnitude fewer counts compared to panel (b). The peak at detector position 765 in panel (c) represents 6+ also with more than two orders of magnitude fewer counts compared to panel (b). Moving the detector to position 830 where 7+ is expected a peak with the number of counts dropping off by more than three orders of magnitude compared to 5+ is shown in panel (d).

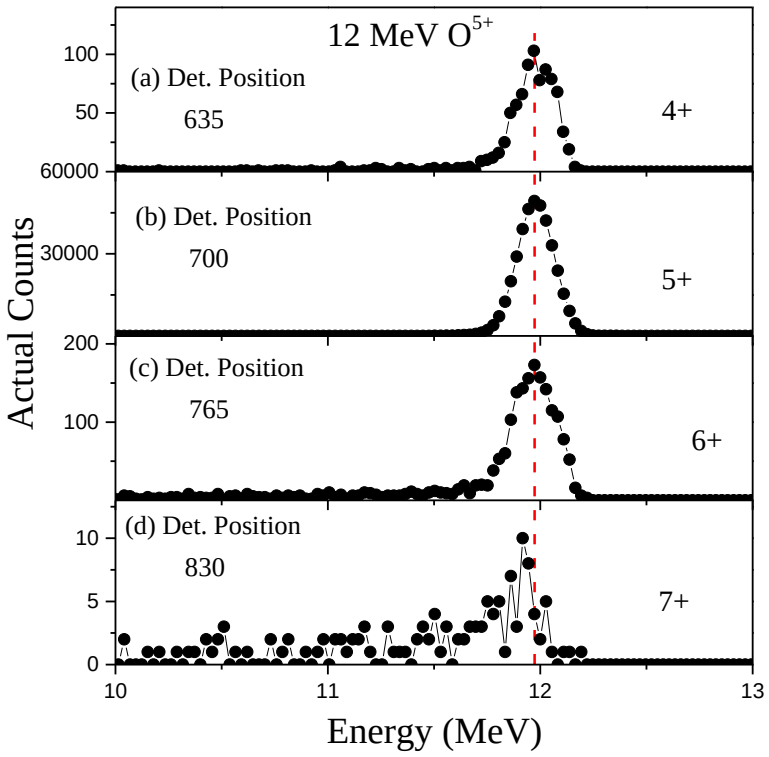

Figure 20. Spectra for 12 MeV O^{5+} ions at tilt angle $\psi = +0.6^{o}$ (measured zero) showing the peak at detector position (a) 635 for 4+, (b) 700 for 5+, (c) 765 for 6+, and (d) 830 for 7+, with the dashed red line drawn at the center of the main peak.

Figure 21 shows the actual counts for 24 MeV O^{5+} as a function of the detected energy obtained also by converting the channel numbers into energy as in figure 19 and 20. Panel (a) shows a symmetric peak representing the main incident beam O^{5+}. The peak shown in panel (b) represents 6+ with about the same energy as the main peak shown in panel (a) and the number of counts is fewer by about two orders of magnitude. Panel (c) shows scattered counts at detector position 830 where 7+ is expected to be, and panel (d) shows scattered counts for detector position 890 where 8+ is expected to be.

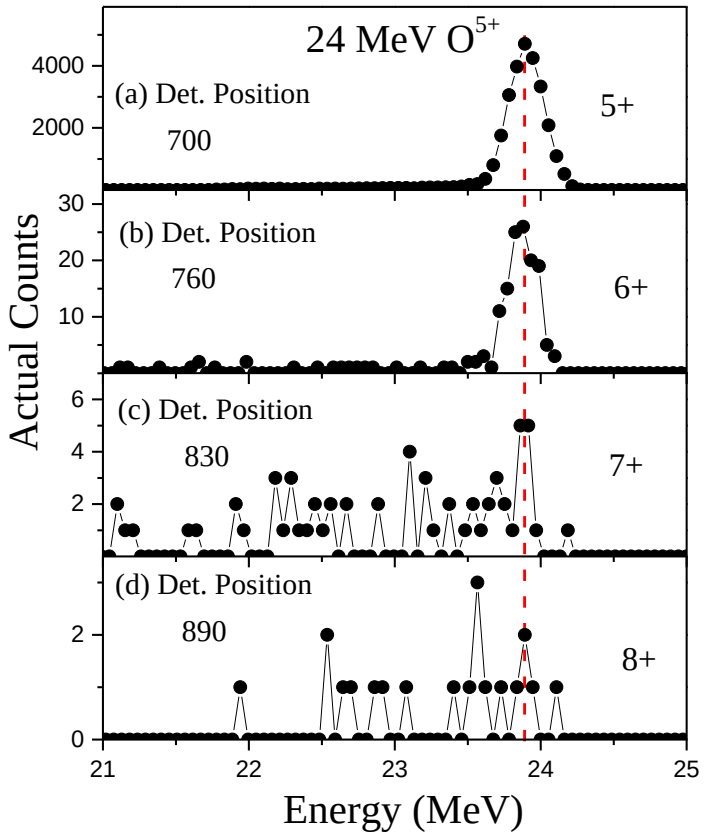

Figure 21. Spectra for 24 MeV O^{5+} ions at tilt angle $\psi = 0.0^{o}$ showing the peak at detector position (a) 700 for 5+, (b) 760 for 6+, (c) 830 for 7+, and (d) 910 for 8+, with the dashed red line drawn at the center of the main peak.

From the actual spectra of 12, 16 and 24 MeV O^{5+} on capillary II the centroid and the FWHM values for each detected charge state were calculated and are shown in table 6. The centroid values show that the peaks representing the transmitted ions are shifted to the left indicating a loss in energy by ~ 0.16% for 12 MeV, 1.4% for 16 MeV and 0.42% for 24 MeV for the primary charged state due to the high counting rates on the detector. Also shown in the table, the incident 12 MeV O^{5+} includes the charge states between 4+ through 7+ with energy losses ~0.18% for 4+ ,~0.25% for 6+ and ~1.25% for

7+. The incident 16 MeV O^{5+} includes the charge states between 4+ through 8+ with energy loss of ~2 % for all detected charge states. Moreover the incident 24 MeV O^{5+} shows the charge states between 5+ and 7+, with less than 1% energy loss for 6+ and about 1.3 % for 7+ also due to the high counting rate at the detector.

Energy	Charge State	Detector Position	Centroid (MeV)	FWHM (MeV)
12 MeV	4+	635	11.98 ± 0.01	0.22 ± 0.01
	5+	700	11.98 ± 0.01	0.20 ± 0.01
	6+	760	11.97 ± 0.01	0.25 ± 0.01
	7+	830	11.85 ± 0.01	0.42 ± 0.02
16 MeV	4+	635	15.72 ± 0.01	0.32 ± 0.01
	5+	700	15.78 ± 0.01	0.25 ± 0.01
	6+	755	15.75 ± 0.01	0.30 ± 0.01
	7+	820	15.70 ± 0.02	0.60 ± 0.02
	8+	890	15.62 ± 0.02	0.68 ± 0.06
24 MeV	5+	700	23.90 ± 0.01	0.29 ± 0.01
	6+	760	23.87 ± 0.01	0.25 ± 0.02
	7+	830	23.66 ± 0.03	0.98 ± 0.06

Table 6. The centroid and FWHM values for incident 12, 16 and 24 MeV O^{5+} ions on straight capillary II.

Figure 22 shows the normalized intensity for the three incident energies as a function of detector position at several tilt angles. The primary incident charge state 5+ has the maximum transmission through the capillary for all incident energies and the corresponding peaks appear to a have narrower spread in detector position units than the other charge states. The intensity falls off by about three orders of magnitude on both sides of the 5+ peak, about two orders of magnitude for 6+ , and about one order for 4+

and 7+. On the other hand 8+ shows the least intensity by about four or five orders of magnitude compared to 5+. Also, 5+ is found to have more transmission compared to 6+ by about two orders of magnitude and three orders compared to 7+. Tilting the sample around the measured zero by small angles does not change the width of the 5+ peak but the intensity falls off on both sides of the peak by about three orders of magnitude for all energies.

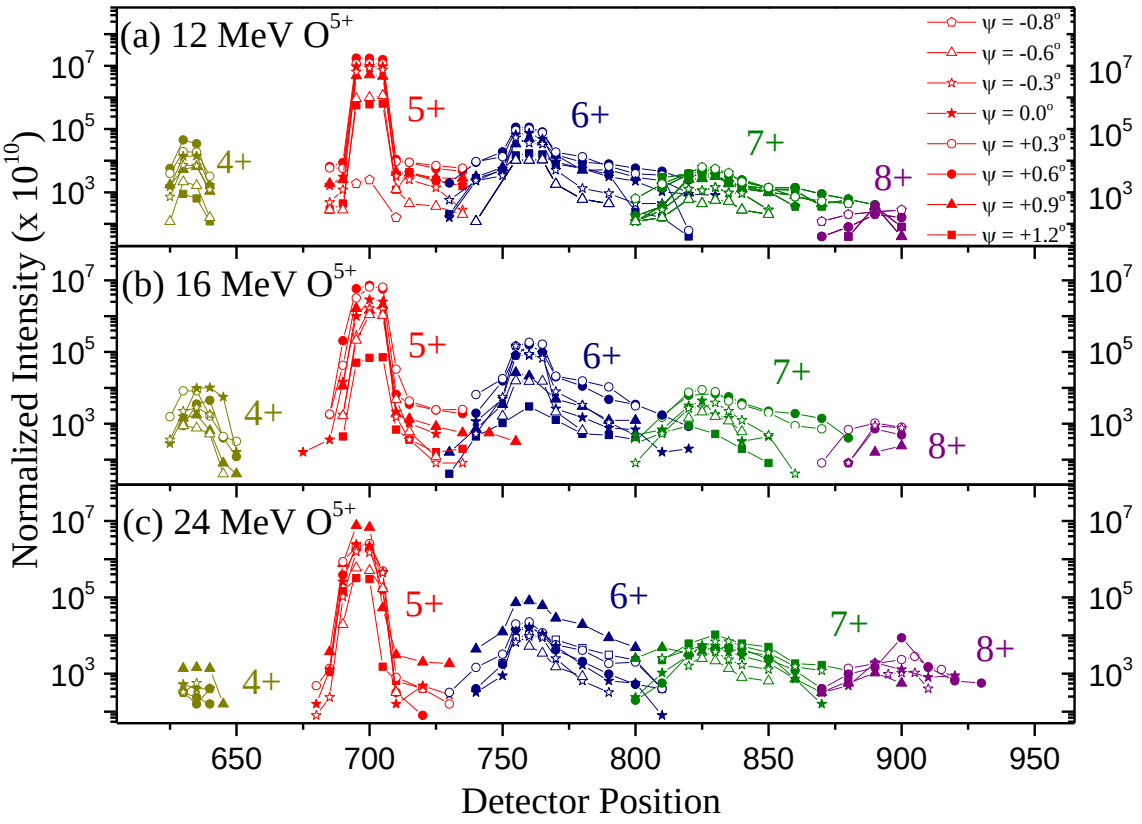

Figure 22. Normalized intensity of the transmitted oxygen through capillary II as a function of detector position at several tilt angles for: (a) 12, (b) 16 and (c) 24 MeV O^{5+} ions.

The captured ions 4+ show more counts at 12 and 16 MeV than at 24 MeV, while the three-electron loss ions (8+) show fewer counts at 12 and 16 MeV compared to 24

MeV as seen in figure 22, which indicates that as the energy increases the intensity for capture (4+) decreases, while for loss (6+ to 8+) the intensity increases as the energy increases. These results agree with the results found by Schlachter et al. (63) which indicates that the single-electron-capture cross sections decrease with increasing energy and with Graham et al. (64) where the electron-loss cross section increase with increasing energy.

Transmission through the Tapered Capillary

The tapered capillary was used with the same set of energies as straight capillary II to compare the results of the two different capillaries for better understanding of the transmission mechanisms. Figures 23, 24 and 25 show the actual counts for 12, 16 and 24 MeV O^{5+}, respectively, as a function of energy, where the channel number was converted into energy as described earlier in chapter III.

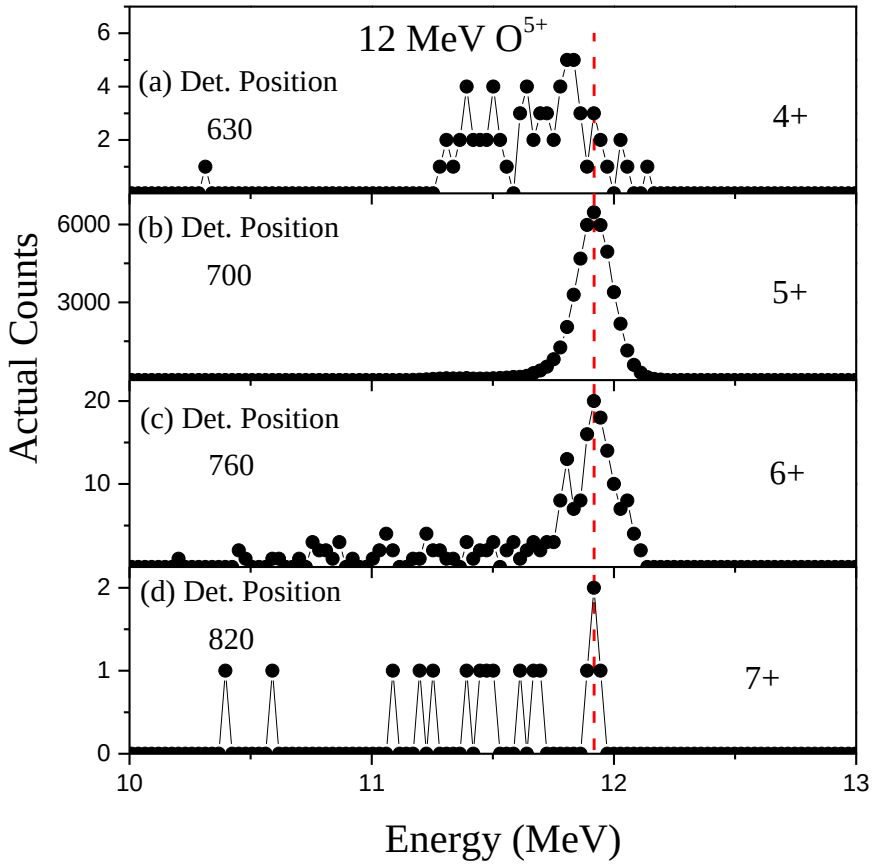

Figure 23. Spectra for 12 MeV O^{5+} ions at tilt angle $\psi = +0.6^{o}$ (measured zero) showing the peak at detector positions: (a) 630 for 4+, (b) 700 for 5+, (c) 760 for 6+, and (d) 820 for 7+, with the dashed red line drawn at the center of the main peak.

Panel (b) in figure 23 shows a symmetric sharp narrow peak at detector position 700 representing the main incident beam. Panel (a) shows a wider peak at detector position 630 that represents 4+ shifted to the left, while panel (c) shows a peak that represents 6+ with about the same energy as the primary beam with more than two orders of magnitude fewer counts compared to the counts in panel (b). At detector position 820 the few scattered counts represent 7+.

In figure 24 panel (b) shows a symmetric peak at detector position 700 with the maximum number of counts representing 5+. Panel (a) shows scattered counts at detector position of 4+, and panel (c) shows a wider peak representing 6+ at detector position 765 with about three orders of magnitude fewer counts compared to 5+. Panels (d) and (e) show scattered counts at detector position 830 and 900 representing 7+ and 8+, respectively.

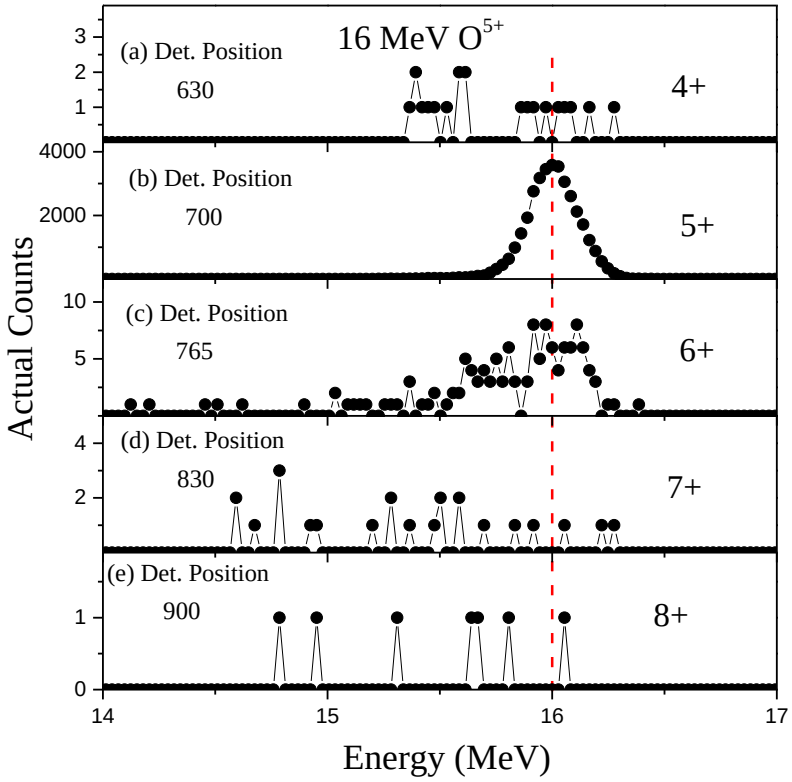

Figure 24. Spectra for 16 MeV O^{5+} ions at tilt angle $\psi = +0.6^{o}$ (measured zero) showing the peak at detector positions: (a) 630 for 4+, (b)700for 5+, (c) 765 for 6+, (d) 830 for 7+, and (e) 900 for 8+, with the dashed red line drawn at the center of the main peak.

The actual counts as a function of energy for 24 MeV O^{5+} are shown in figure 25 with panel (a) showing a nearly symmetric peak at detector position 700 with a tail to the

left representing the primary charge state 5+. At detector position 765 in panel (b) the statistics represents 6+ with the same energy as the primary beam and the number of counts dropping off by about three orders of magnitude. Panels (c) and (d) show scattered counts at detector positions 840 and 900 representing 7+ and 8+, respectively.

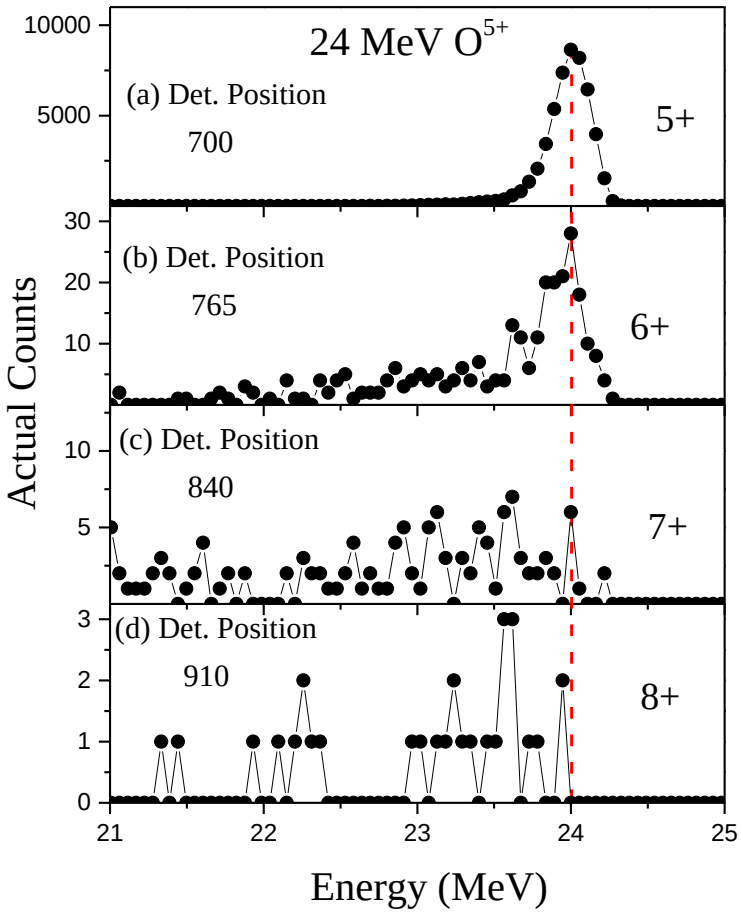

Figure 25. Spectra for 24 MeV O^{5+} ions at tilt angle $\psi = +0.6^{o}$ (measured zero) showing the peak at detector positions: (a) 700 for 5+, (b) 765 for 6+, (c) 840 for 7+, and (d) 910 for 8+, with the dashed red line drawn at the center of the main peak.

The centroid values show that the peaks representing the transmitted ions are shifted slightly to the left indicating a loss in energy by less than 1% for the detected 5+

and 6+ charge states and ~ 2% for 4+ at 12 MeV due to the high counting rate on the detector. The FWHM values have the narrowest width for 5+ compared to the other detected charge states for all the used energies.

Energy	Charge state	Detector Position	Centroid (MeV)	FWHM (MeV)
12 MeV	4+	630	11.69 ± 0.02	0.58 ± 0.02
	5+	700	11.92 ± 0.01	0.18 ± 0.01
	6+	760	11.92 ± 0.02	0.24 ± 0.01
16 MeV	5+	700	16.00 ± 0.01	0.26 ± 0.01
	6+	765	15.93 ± 0.01	0.56 ± 0.01
24 MeV	5+	700	24.00 ± 0.01	0.29 ± 0.01
	6+	765	23.93 ± 0.01	0.42 ± 0.02

Table 7. The centroid and FWHM values for incident 12, 16 and 24 MeV O^{5+} ions on the tapered capillary.

Figure 26 shows the normalized integrated intensity for all incident energies as a function of detector position at several tilt angles. The primary incident charge state (5+) has the maximum transmission through the capillary for all energies. The intensity falls off by about four orders of magnitude on both sides of the 5+ peak, less than two orders of magnitude for 6+, and less than about one order of magnitude for 7+ at 12 and 16 MeV, whereas 7+ has about the same intensity as 6+ at 24 MeV and the drop off is about two orders of magnitude on both sides of the peak. For 4+ a peal appears strongly at 12 MeV and the counts fall off by about one order of magnitude. A peak for 8+ appears at 16 and 24 MeV but is stronger at 24 MeV.

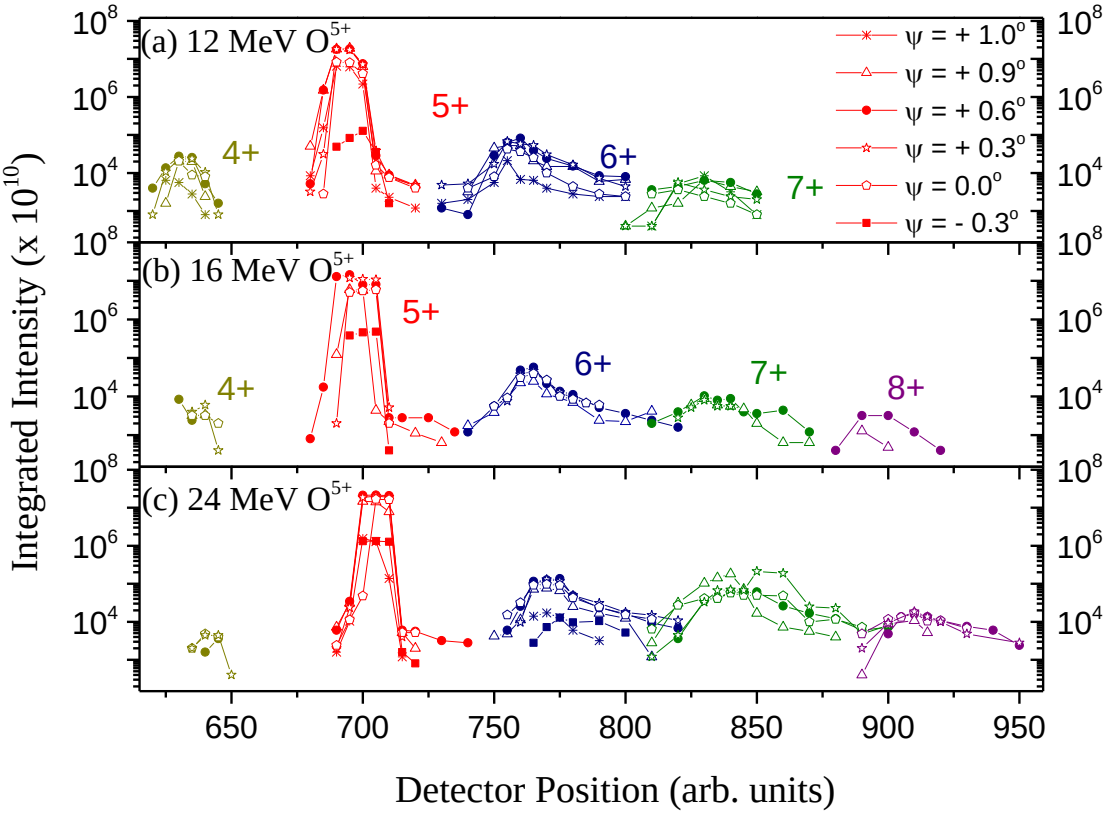

Figure 26. Normalized intensity of the transmitted oxygen ions through the tapered capillary as function of detector position at several tilt angles for: (a) 12 (b) 16 and (c) 24 MeV O^{5+}

Figure 27 shows the FWHM in terms of detector position as a function of tilt angle for all the energies used for the straight and the tapered capillaries. Panels (a) and (c) show that the FWHM values are the same within uncertainties for the primary charge state 5+ at all the energies for the straight and tapered capillaries. Panels (b) and (d) show that the FWHM for the next higher charge state 6+ is about the same for all the energies used for the same capillary, it is wider compared to the primary charge state, and also the tapered capillary has a wider width compared to the straight capillary.

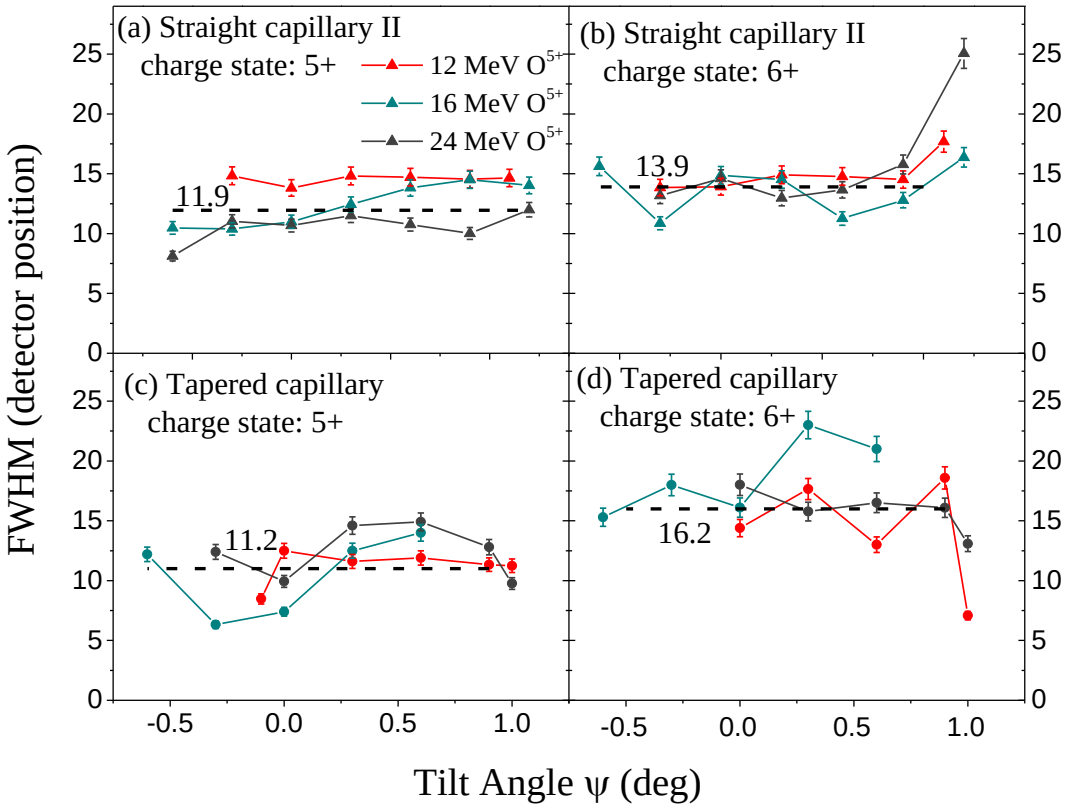

Figure 27. The FWHM as a function of tilt angle ψ (deg) for 12, 16 and 24 MeV O^{5+} ions for (a) 5+ and (b) 6+ for the straight capillary and (c) 5+ and (d) 6+ for the tapered capillary.

Figure 28 shows the integrated peak intensity as a function of tilt angle for 12, 16 and 24 MeV for the straight capillary in the upper panels and for the tapered capillary in the lower panels. For the straight capillary the peak intensity drops off by a factor of three in changing the energy from 12 to 16 MeV as shown in panels (a) and (b), and from 16 to 24 the peak intensity falls off again by a factor of two as seen in panels (b) and (c). For the tapered capillary shown in the lower panels the peak intensities are about the same for all the energies taking into account the peaks width.

The FWHM values for all the incident energies are about the same within the uncertainties for the straight capillary as shown in panels (a), (b) and (c). Also it is the same within uncertainties for the tapered capillary as seen in panels (d), (e) and (f). Moreover, the straight capillary shows a wider width in terms of tilt angle compared to the tapered capillary.

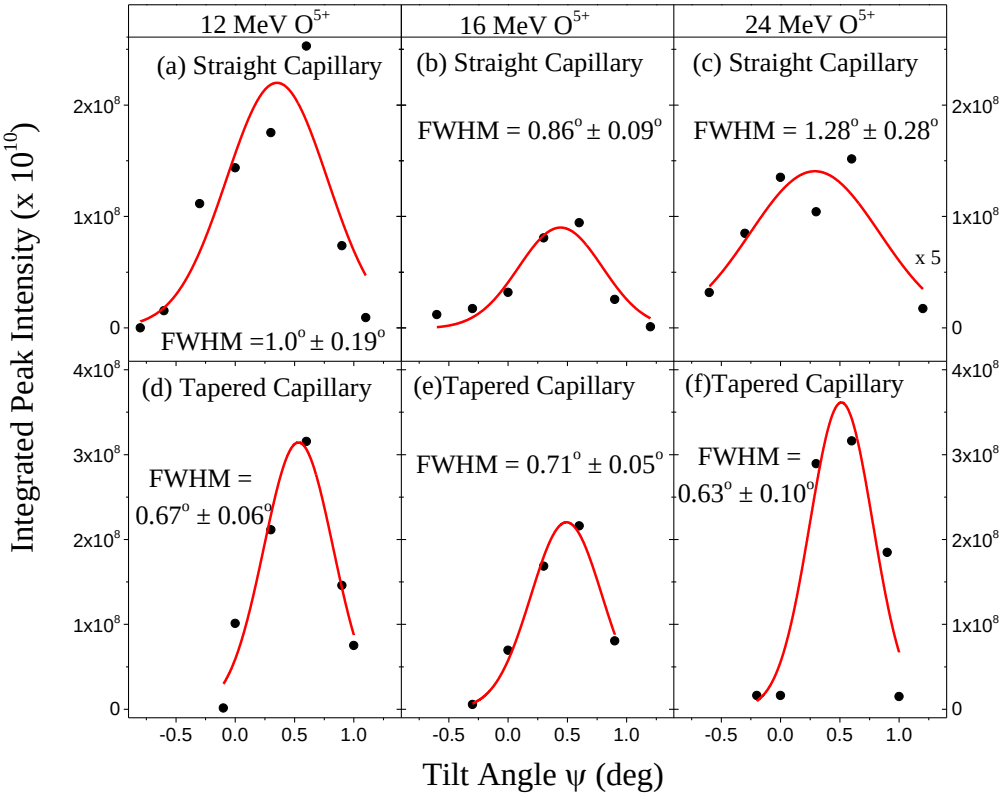

Figure 28. The integrated peak intensity as a function of tilt angle ψ (deg) for the straight capillary at (a)12 (b)16 and (c) 24 MeV (multiplied by a factor of 5), and for the tapered capillary at (d) 12 (e) 16 and (f) 24 MeV, with the solid red line indicating the results of a Gaussian fit.

The integrated area of each detected charge state for both capillaries is shown as a function of energy in the figure 29. As the energy increases the peak area decreases for the capture events in both capillaries as seen in panel (a). Panel (b) shows that the primary incident charge state (5+) increases for the tapered capillary and decreases for

the straight capillary and the same occurs for (6+) and (7+) as seen in panels (c) and (d) which agrees with the results from Refs (63,64) for capture and loss as discussed earlier in this chapter.

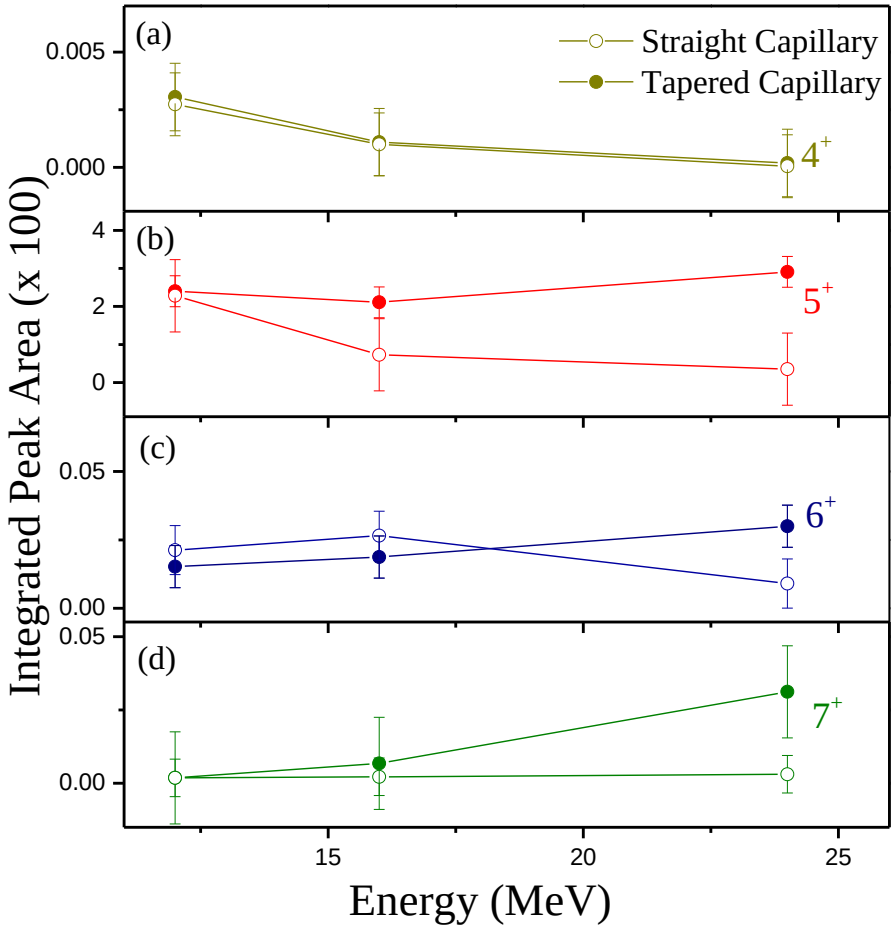

Figure 29. The integrated peak area for the straight and tapered capillaries as a function of energy for O^{5+} as the primary incident charge state.

Charge State Dependence

As mentioned earlier the charge state dependence was studied using the tapered glass capillary where the incident energy was fixed at 16 MeV and the incident

charge state was varied from 5+ to 8+. The normalized intensities as a function of detector position for 16 MeV O^{5+} through O^{8+} are shown in figure 30.

The intensities for the primary incident charge states are shown as: panels (a) 5+, (b) 6+, (c) 7+ and (d) 8+. The transmitted intensity for the primary incident charge state is $2x10^7$ in each panel. Also the intensity of the main peak (primary charge) falls off by about four orders of magnitude at the peak sides in each panel. For each primary incident charge state there is only one captured electron due to the speed of the incident ion, i.e., for 5+ as the primary incident ion 4+ is the only captured ion and for 6+ as the primary incident ion 5+ is the only captured ion. The intensity of the captured ion is less than the primary incident ion by three orders of magnitude for the incident charges 5+ and 6+ as shown in panels (a) and (b), and about two orders of magnitude for 7+ and 8+ as shown in panels (c) and (d). On the other hand, each primary incident charge state has a loss depending on how many electrons it can lose, i.e., 5+ can lose 3 electrons, 6+ can lose 2 electrons and 7+ can lose only one electron. The intensity of the first lost ion is about two orders of magnitude less in panel (a); it is about three orders less in panel (b) and about four orders less in panel (c). The second lost electron has a drop in intensity by about three orders of magnitude in panel (a) with 5+ as the primary charge and about four orders of magnitude in panel (b) with 6+ being the primary charge. Panel (a) shows the only third lost electron with a drop in intensity by about four orders of magnitude compared to the primary charge 5+.

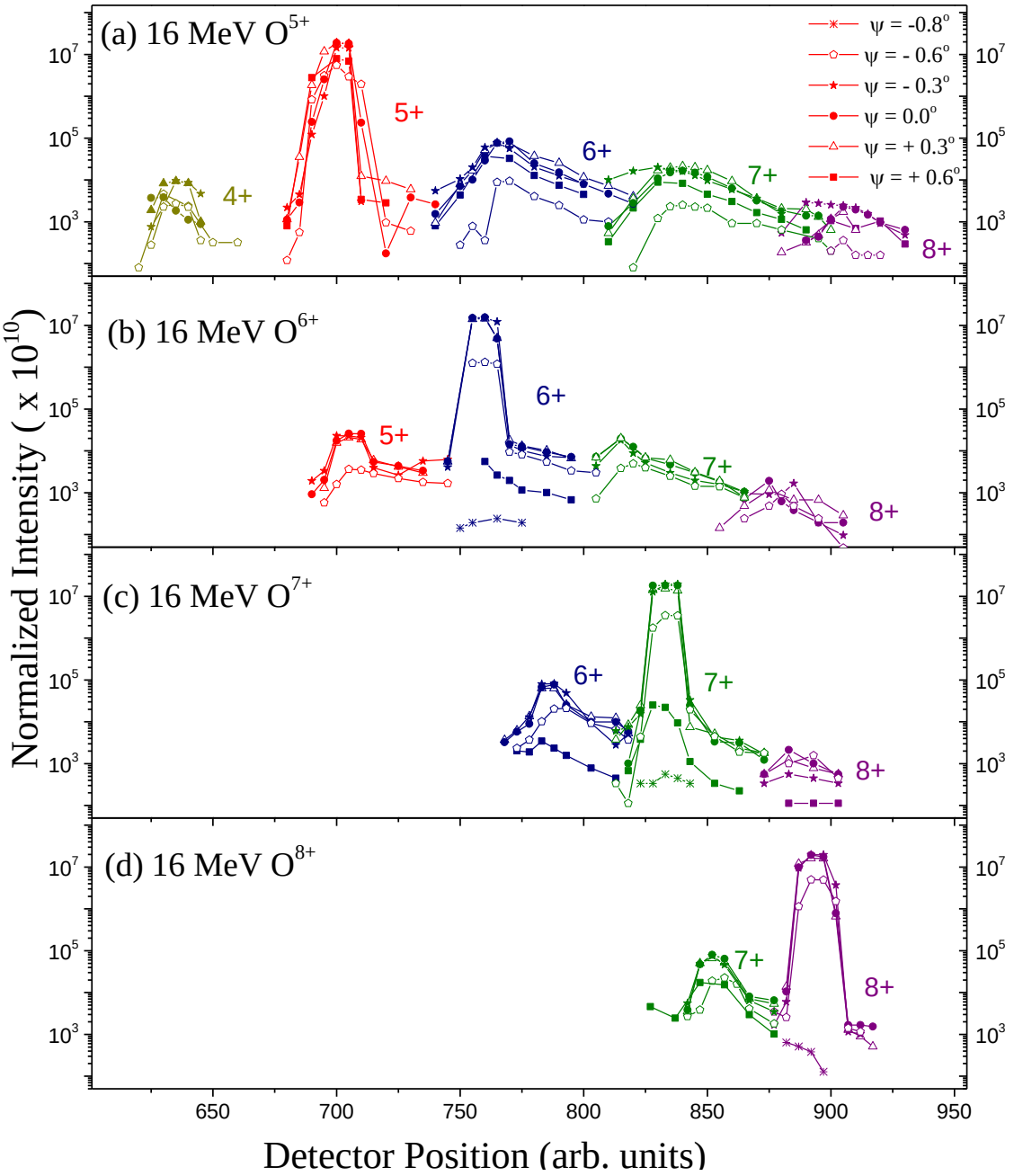

Figure 30. Normalized intensity as a function of detector position for 16 MeV oxygen: (a) 5+, (b) 6+, (c) 7+ and (d) 8+.

Figure 31 shows the integrated peak areas as a function of incident charge state for 16 MeV O^{q+}. As seen in the figure the incident charge state increases the area of the capture increases, and the area of the loss decreases which agrees with Ref. (64).

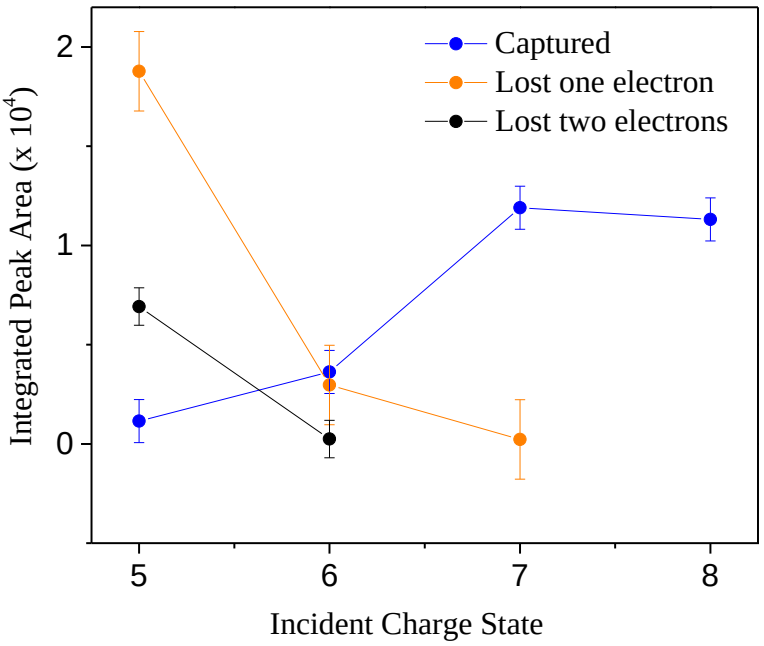

Figure 31. The integrated peak area as a function of incident charge state for 16 MeV O^{q+}.

The FWHM for each peak in figure 30 in terms of detector position is plotted as a function of tilt angle ψ (deg) in figure 32. Panel (a) shows the primary incident charge state, panel (b) shows the capture and panels (c) and (d) show the first and second lost electrons. The FWHM is about 12 units (~0.40 cm) for the primary incident charge state which is less than the slit width (~0.7 cm). The captured ion width is ~ 14 units (~ 0.46 cm) and the first loss width is ~19 units (~ 0.63 cm) which is about the slit width. The second lost is even wider ~ 24 units (~0.79 cm) as seen in the figure which is more than the slit width.

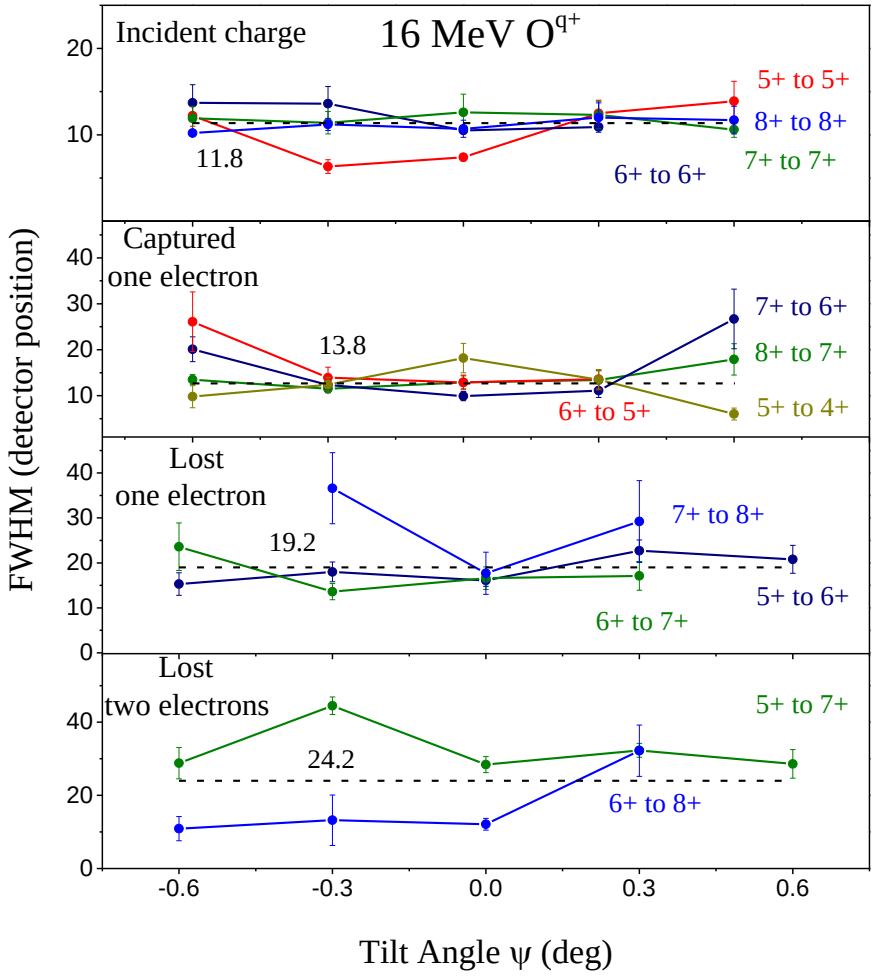

Figure 32. The FWHM in detector position units as a function of tilt angle ψ (deg) for 16 MeV O^{5+} ions.

Figure 33 shows the integrated peak intensity as a function of tilt angle for 1 MeV protons in the upper panel and 16 MeV/u O^{8+} in the lower panel for the tapered capillary. The FWHM values are the same within uncertainties for both beams and also the peak intensity is about the same. These results indicate that the transmission of protons and oxygen ions through tapered capillary is about the same.

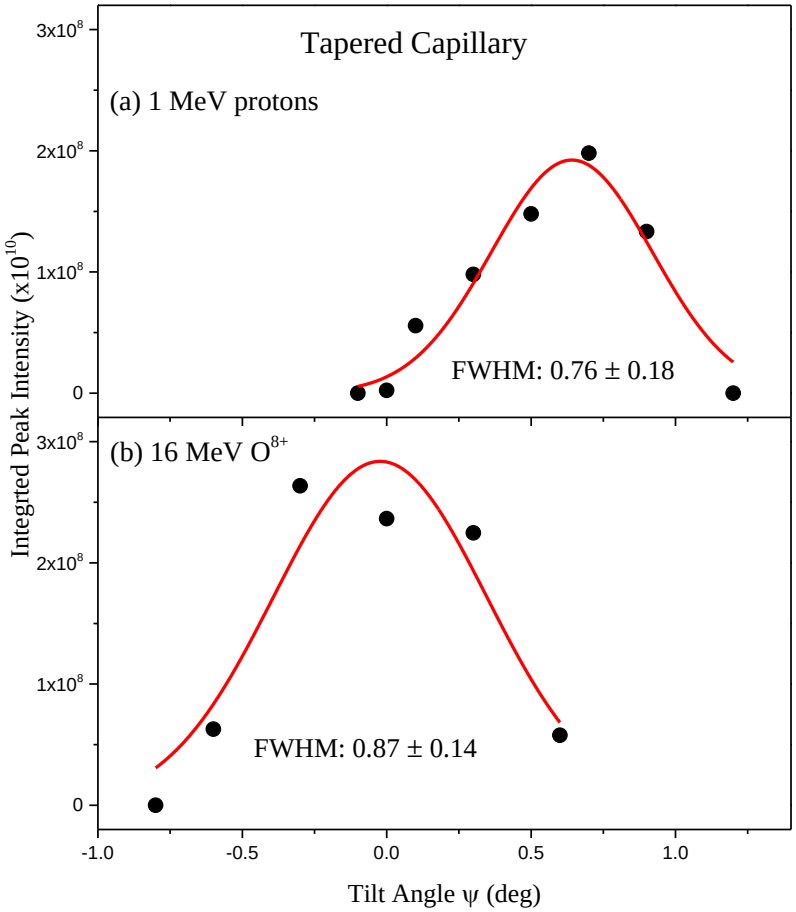

Figure 33. The integrated peak intensity as a function of tilt angle ψ (deg) for the tapered capillary for (a)1 MeV protons and (b) 16 MeV O^{8+} ions, with the solid red line indicating the results of Gaussian fits.

Transmission Factor

Several techniques were used to enhance or focus slow and fast ion beams due to the potential applications as mentioned in chapter II. Recently a tapered glass capillary was used to focus 2 MeV He^{+} ions (11) and the results show that the beam density can be enhanced without significant energy loss. In this section the transmission factor for 1 and 3 MeV protons and 12, 16 and 24 MeV O^{5+} ions through the straight and tapered capillaries is calculated as well as showing a comparison between the two capillaries.

The transmission factor (*T*) is the ratio of the transmitted current density to the incident current density given by the following formula:

$$T = \frac{J_{out}}{J_{in}} = \frac{(I_O / I_i)}{(r_o/r_i)^2} \quad (3)$$

The parameters used are defined as:

I_i: the incident current

I_o: the transmitted current

r_i: the inlet radius

r_o: the outlet radius

The outlet area to the inlet area for the straight capillary is unity and for the tapered capillary it is 20 x 10^{-3}. The transmission factor calculations for 16 MeV O^{5+} on the tapered capillary are shown below:

$$I_i = \left(\frac{r_{cap}}{r_{col}}\right)^2 \times I_s = 0.15 \text{ x } 10^{-12}\text{A} \quad (4)$$

r_{cap}: the capillary inlet radius

r_{col}: the collimator radius

I_s: current on the sample

$$I_o = \frac{N \times qe}{t} = 0.61 \text{ x } 10^{-15}\text{A} \quad (5)$$

E: the electron charge (1.6 x10^{-19} C)

q: the incident charge, 1 for protons and 5 for oxygen ions

t: time (sec)

Then the output current density to the input current density ratio is:

$$T = \frac{0.61 \times 10^{-15} A / 0.15 \times 10^{-12} A}{20 \times 10^{-3}} = 0.20$$

The same method was used to calculate *T* for the straight and tapered capillaries for all the energies investigated for the protons and the oxygen ions. The transmission factor percentage values are shown in table 8 and plotted as a function of energy in figure 34.

Beam	Capillary	Energy (MeV)	Transmission factor %
Proton	Straight	1	23
		3	11
	Tapered	1	12
		3	19
Oxygen	Straight	12	12
		16	3
		24	8
	Tapered	12	12
		16	20
		24	24

Table 8. The transmission factor in percent for all the energies used on the straight and tapered capillaries. The uncertainties in the transmission factor is estimated to be ~15% due to all sources of error.

As shown in figure 34 panel (a) the transmission factor decreases with increasing energy for the straight capillary and increases with increasing energy for the tapered capillary for protons. On the other hand, the transmission factor is about the same for 12 MeV/u O^{5+} (0.75 MeV) for the straight and tapered capillaries, then it increases with

increasing energy for the tapered capillary and decreases for the straight capillary as for protons.

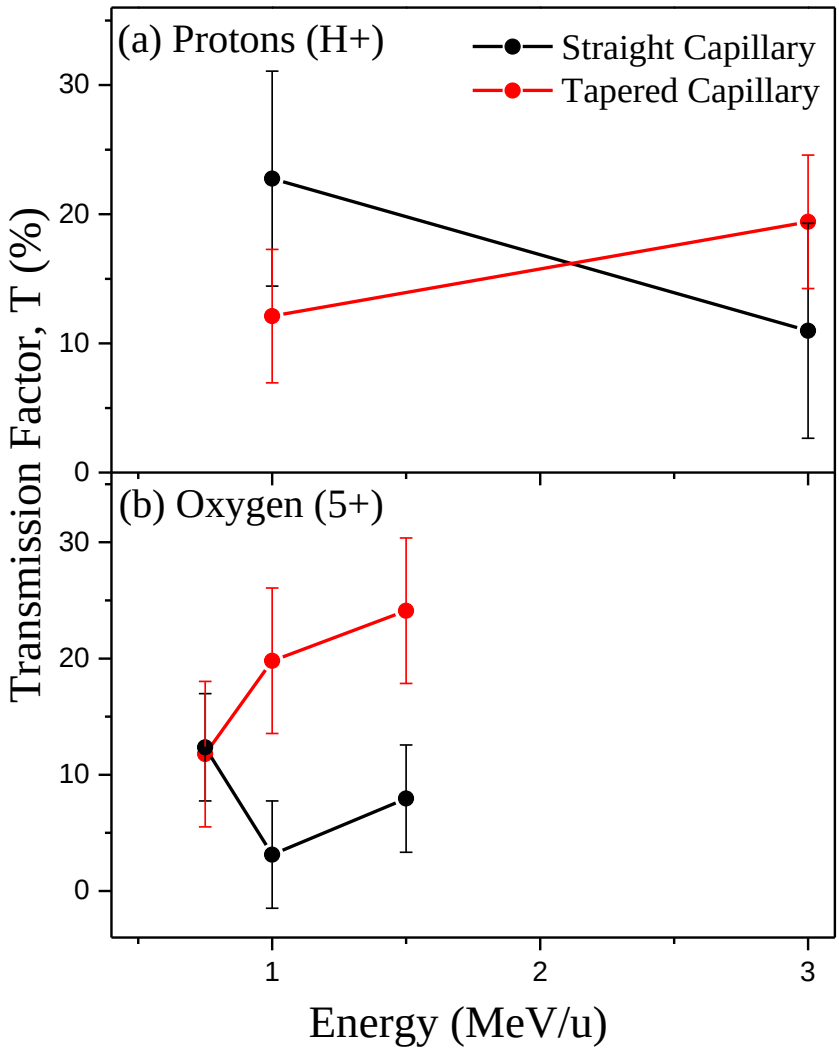

Figure 34. The transmission factor in percentage as a function of energy in MeV/u for the straight and tapered capillaries for: (a) protons and (b) oxygen ions.

CHAPTER V

CONCLUSION

The interaction of fast protons and oxygen ions with insulating single straight- and funnel-shaped glass capillaries of microscopic dimensions was investigated in this work to understand the transmission mechanisms. Protons and oxygen ions were used with variable energies and variable charge states for the oxygen ions, in order to understand the transmission energy dependence and charge state dependence using both capillaries.

Fast protons and oxygen ions traverse the straight and tapered glass capillaries with no significant energy loss and the results were reproducible for the used energies. The protons transmission was higher for the lower energy, i.e, 1 MeV, in both capillaries, although the transmission through the straight capillary was higher due to its size and shape. The oxygen results for the straight capillary showed that the transmission at the lower energy is higher compared to the high energy and the same is for protons. However, the transmission through the tapered capillary was about the same for all the used energies. The transmission FWHM values in terms of angle (degrees) is about the same within uncertainties for protons and oxygen ions at all the energies used for the straight capillary and the same true for the tapered capillary. Never the less, the tapered capillary showed a narrower width because of its shape. The transmission FWHM in terms of detector position (displacement) is about the same in both capillaries for all the used energies.

The charge state dependence study showed that the primary incident charge state $(q)^+$ had the maximum transmission through the tapered capillary. The first lost electron $(q+1)^+$ had the next highest transmission and only one captured electron $(q-1)^+$ was possible. The peak widths in terms of displacement show that the width for charge changed probabilities were broader than for the primary incident charge estate. The width of charge changed cross section went in ascending from capture to one electron loss and two electron loss.

The transmission factor values indicates that as the energy increases the transmission factor increases using the tapered capillary and it decreases using the straight capillary. For better understanding another tapered capillary with different dimensions should be used to prove this result with higher energies.

BIBLIOGRAPHY

1. J. P. Briand, L. de Billy, P. Charles, S. Essabaa, P. Briend, R. Geller, J. P. Desclaux, S. Bilman, and C. Ristori, *Production of hollow atoms by the excitation of highly charged ions in interaction with a metallic surface*, Phys. Rev. Lett. **65**, 159 (1990).

2. K. Tökési, L. Wirtz, C. Lemell, and J. Burgdörfer, *Charge-state evolution of highly charged ions transmitted through microcapillaries,* Phys. Rev. A **61**, 020901 (2000).

3. N. Stolterfoht, J. H. Bremer, V. Hoffmann, R. Hellhammer, D. Fink, A. Petrov, and B. Suilk, *Transmission of 3 keV Ne^{7+} ions through nanocapillaries etched in polymer foils: evidence for capillary guiding*, Phys. Rev. Lett. **88,** 133201 (2002).

4. K. Schiessl, W. Palfinger, K. Tőkési. H. Nowotny, C. Lemell, and J. Burgdörfer, *Simulation of ion guiding through insulating capillaries: Effects of inter-capillary interaction*, Nucl. Instr. and Meth. Phys. Res. B **258**, 150 (2007).

5. Y. Iwai, T. Ikeda, T. M. Kojima and Y. Yamazaki, *Ion irradiation in liquid of μm3 region for cell surgery*, App. Phys. Lett. **92,** 023509 (2008).

6. D. Sekiba, H. Yonemura, S. Ogura, M. Matsumoto, Y. Kitaoka, Y. Yokoyama, H. Matsuzaki, T. Narusawa, and K. Fukutani, *Development of micro-beam NRA for hydrogen mapping: Observations of fatigue-fractured surface of glassy alloys,* Nucl. Instr. and Meth. Phys. Res. B **269**, 627 (2011).

7. Y. Yamazaki, *Production of hollow atoms (ions) in HCI-surface collision*, Phys. Scr. T **73**, 293 (1997). Y. Yamazaki, *Beam capillary spectroscopy*, Int. Jour. of mass Spec. **192,** 437 (1999). Y. Yamazaki, *Interaction of slow highly-charged ions with metals and insulators*, Nucl. Instr. and Meth Phys. Res. B **258**, 139 (2007).

8. S. Ninomiya, Y. Yamazaki, F. Koike, H. Masuda, T. Azuma, K. Komaki, K. Kuroki, and M. Sekiguchi, *Stabilized hollow ions extracted in vacuum*, Phys. Rev. Lett. **78**, 4557 (1997).

9. Y. Yamazaki, *A microcapillary target as a metastable hollow ion source*, Nucl. Instr. and Meth. in Phys. Res. B **193**, 516 (2002).

10. N. Stolterfoht, R. Hellhammer, J. Bundesmann, D. Fink, Y. Kanai, M. Hoshino, T. Kambara, T. Ikeda, and Y. Yamazaki, *Guiding of slow Ne^{7+} ions through nanocapillaries in insulating polyethylene terephthalate: Incident current dependence*, Phys. Rev. A **76**, 022712 (2007).

11. T. Nebiki, T. Yamamoto, T. Narusawa, M. B. H. Breese, E. J. Teo, and F. Watt, *Focusing of MeV ion beams by means of tapered glass capillary optics*, J. Vac. Sci. Technol. A **21**, 1671 (2003).

12. F. Aumayr, HP. Winter, *Inelastic interactions of slow ions and atoms with surfaces*, Nucl. Instr. and Meth. Phys. Res. B **233**, 111(2005).

13. J. F. Ziegler, J. P. Biersack, U. Littmark, *The Stopping and Range of Ions in Matter*, *Pergamon*, New York (1985).

14. W. M. Arnoldbik, N. Tomozeiu and F.H.P.M. Habraken, *Electronic sputtering of thin SiO_2 films by MeV heavy ions*, Nucl. Instr. and Meth. Phys. Res. B **203**, 151 (2003)

15. N. Stolterfoht, V. Hoffmann, R. Hellhammer, Z. D. Pešić, D. Fink, A. Petrov, and B. Sulik, *Guided transmission of 3 keV Ne^{7+} ions through nanocapillaries etched in a PET polymer*, Nucl. Instr. and Meth. in Phys. Res. B **203**, 246 (2003).

16. P. Skog, HQ. Zhang, and R. Schuch, *Evidence of sequentially formed charge patches guiding ions through nanocapillaries*, Phys. Rev. Lett. **101**, 223202 (2008).

17. K. Schiessl, W. Palfinger, K. Tőkési, H. Nowotny, C. Lemell, and J. Burgdörfer, *Simulation of guiding of multiply charged projectiles through insulating capillaries*, Phys. Rev. A **72**, 062902 (2005). K. Schiessl, W. Palfinger, C. Lemell, J. Burgdörfer, *Simulation of guiding of highly charged projectiles through insulating nanocapillaries*, Nucl. Instr. and Meth. in Phys. Res. B **232**, 228–234 (2005).

18. Y. Kanai, M. Hoshino,T. Kambara,T. Ikeda,R. Hellhammer, N. Stolterfoht, and Y. Yamazaki, *Dynamic features of ion guiding by nanocapillaries in an insulating polymer*, Phys. Rev. A **79**, 012711 (2009).

19. N. Stolterfoht, R. Hellhammer, D. Fink, B. Sulik , Z. Juhász, E. Bodewits, H. M. Dang, and R. Hoekstra, *Dynamic properties of ion guiding through nanocapillaries in an insulating polymer*, Phys. Rev. A **79**, 022901(2009).

20. H. Q. Zhang, P. Skog and R. Schuch. *Dynamics of guiding highly charged ions through SiO_2 nanocapillaries*, Phys. Rev. A **82**, 052901 (2010).

21. R. Hellhammer, P. Sobocinski, Z. D. Pešić, J. Bundesmann, D. Fink and N. Stolterfoht, *Interaction of slow highly charged ions with the inner surface of nanocapillaries*, Nucl. Inst. and Meth. Phys. Res. B **232**, 235 (2005). R. Hellhammer, Z. D. Pešić, P. Sobocinski, D. Fink, J. Bundesmann and N. Stolterfoht, *Guided transmission of highly charged ions through nanocapillaries in*

PET: Study of the energy dependence. Nucl. Instr. and Meth. Phys. Res. B **233**, 213 (2005).

22. N. Stolterfoht, *Simulation and analysis of ion guiding through a nanocapillary in insulating polymers*, Phys. Rev. A **87**, 012902 (2013).

23. N.Stolterfoht, R. Hellhammer , Z. Juhász, B. Suilk, E. Bodewits, H. M. Dang and R. Hoekstra, *Guided transmission of 3 KeV Ne7+ ions through nanocapillaries in insulating polymers: Dependence of the capillary diameter*, Phys. Rev. A **82**, 052902 (2010).

24. K. Schiessl, W. Palfinger, K. Tőkési. H. Nowotny, C. Lemell, and J. Burgdörfer, *Simulation of ion guiding through insulating capillaries: Effects of inter-capillary interaction*, Nucl. Instr. and Meth Phys. Res. B **258**, 150 (2007). K. Schiessl, C. Lemell, K. Tőkési and J. Burgdörfer, *Energy dependence of ion guiding through nanocapillaries*, J. of Phys.: Conf. Ser.**163**, 012081 (2009).

25. C. Lemell, K. Schiessl, H. Nowotny and J. Burgdörfer, *Simulation of heavy-ion guiding in insulators*, Nucl. Instr. and Meth. Phys. Res. B **256**, 66 (2007).

26. G. P. Pokhil, K. A. Vokhmyanina, L. A. Zhilyakov, T. Ikeda, Y. Kanai, Y. Iwai, T. M. Kojima , and Y. Yamazaki, *Ion Guiding through a Flat Insulating Channel*, ISSN 1062-8738, Bulletin of the Russian Academy of Sc.: Phys. Vol. **72**, No. 5, 638 (2008).

27. Y. Kanai, M. Hoshino, T. Kambara, T. Ikeda, R. Hellhammer, N. Stolterfoht, and Y. Yamazaki, *Two-dimensional images of transmitted slow neon ions guided by nanocapillaries in polymer foils*, Nucl. Instr. and Meth. Phys. Res. B **258**, 155 (2007).

28. R. Hellhammer, D. Fink and N. Stolterfoht, *Guiding of highly charged ions through nanocapillaries in PET: Dependence on the projectile energy and charge*, Nucl. Instr. and Meth. Phys. Res. B **261,**149 (2007).

29. N. Stolterfoht, R. Hellhammer, J. Bundesmann and D. Fink, *Scaling laws of guiding of highly charged ions through nanocapillaries in an insulating polymer*. Phys. Rev. A **77**, 032905 (2008).

30. M. Kreller, G. Zschornack and U. Kentsch. *Guiding of argon ions through PET nano capillary foils*, Jour. of Phys.: Conf. Ser. **163** 012090 (2009).

31. M. B. Sahana, P. Skog, Gy. Vikor, R. T. Kumar, and R. Schuch, *Guiding of highly charged ions by highly ordered SiO2 nanocapillaries*, Phys. Rev. A **73**, 040901 (2006).

32. D. H. Li, Y.Y. Wang, Y.T. Zhao, G.Q. Xiao, D. Zhao, Z.F. Xu and F.L. Lic, *The influence of the charged back side on the transmission of highly charged ions through PC nanocapillaries*, Nucl. Instrum. Methods Phys. Res. B **267,** 469 (2009).

33. N. Stolterfoht, R. Hellhammer, Z. Juhász, B. Sulik, V. Bayer, C. Trautmann, E. Bodewits, A. J. de Nijs, H. M. Dang, and R. Hoekstra, *Guided transmission of Ne^{7+} ions through nanocapillaries in insulating polymers: Scaling laws for projectile energies up to 50 keV*, Phys. Rev. A **79**, 042902 (2009).

34. X. Wang, Y. Zhou, Y. Wang, R. Cheng, D. Li, S. Zhang and G. Xiao, *A study of highly charged ions transmission through polycarbonate nanocapillaries with muliti-holes*, Phys. Scr. T **144**, 014046 (2011).

35. H. F. Krause, C. R. Vane, and F. W. Meyer, *Ions transmitted through an anodic nanocapillary array*, Phys. Rev. A **75**, 042901 (2007).

36. G. Sun, X. Chen, J. Wang, Y. Chen, J. Xu, C. Zhou, J. Shao, Y. Cui, B. Ding, Y. Yin, X. Wang, F. Lou, X. Lv, X. Qiu, J. Jia, L.Chen, F. Xi, Z. Chen, L. Li, and Z. Liu, *Interaction of 18-keV O^- ions with Al_2O_3 nanocapillaries*, Phys. Rev. A **79**, 052902 (2009)

37. R. J. Bereczky, G. Kowarik, F. Aumayr, and K. Tőkési, *Transmission of 4.5 keV Ar^{9+} ions through a single macro-capillary*, Nucl. Instrum. Methods Phys. Res. B **267**, 317 (2009).

38. K. A. Vokhmyanina, L. A. Zhilyakov, A. V. Kostanovsky, V. S. Kulikauskas, V. P. Petukhov and G. Pokhil, *Transportation and focusing of accelerated proton beams by means of dielectric channels*, J. Phys. A: Math. Gen. **39**, 4775 (2006).

39. T. Ikeda, Y. Kanai, T. M. Kojima, Y. Iwai, T. Kambara, Y. Yamazaki, M. Hoshino, T. Nebiki and T. Narusawa, *Production of a microbeam of slow highly charged ions with a tapered glass capillary*, App. Phys. Lett. **89**, 163502 (2006).

40. M. Kreller, G. Zschornack and U. Kentsch, *Guiding of argon ions through a tapered glass capillary*, Nucl. Instr. and Meth. in Phys. Res. B **269**, 1032 (2011).

41. A. Cassimi, L.Maunoury, T. Muranaka, B. Huber, K. R. Dey, H. Lebius, D. Lelièvre, J. M. Ramillon, T. Been, T. Ikeda, Y. Kanai, T. M. Kojim, Y. Iwa, Y. Yamazaki, H. Khemliche, N. Bundaleski and P. Roncin, *Imaging dynamics of charge-auto-organisation in glass capillaries*, Nucl. Inst. and Meth. Phys. Res. B **267**, 674 (2009).

42. T. Ikeda, Y. Kanai, T.M. Kojima, Y. Iwai, Y. Kanazawa, M. Hoshino, T. Kobayashi, G.P. Pokhil and Y. Yamazaki, *Focusing of charged particle beams with various glass-made optics*, J. of Phys.: Conf. Ser. **88**, 012031 (2007).

43. A. R. Milosavljević, Gy. Víkor, Z. D. Pešić, P. Kolarž, D. Šević, B. P. Marinković, S. Mátéfi-Tempfli, M. Mátéfi-Tempfli, and L. Piraux, *Guiding of low-energy electrons by highly ordered Al_2O_3 nanocapillaries*, Phys. Rev. A **76**, 042716 (2007).

44. S. Das, B. S. Dassanayake, M. Winkworth, J. L. Baran, N. Stolterfoht, and J. A. Tanis, *Inelastic guiding of electrons in polymer nanocapillaries*, Phys. Rev. A **76**, 042716 (2007).

45. W. Wang, D. Qi, D. Yu, M., Zhang, F. Ruan, J. Chen and X. Cai, *Transmission of low-energy electrons through SiO_2 tube*, J.. of Phys.: Con. Ser. **163,** 012093 (2009).

46. B. S. Dassanayake, S. Das, R. J. Bereczky, k. Tőkési, and J. A. Tanis, *Energy dependence of electron transmission through a single glass macrocapillary*, Phys. Rev. A **81**, 020701 (2010). B. S. Dassanayake, R. J. Bereczky, S. Das, A. Ayyad, K. Tőkési , and J. A. Tanis, *Time evolution of electron transmission through a single glass macrocapillary: Charge build-up, sudden discharge, and recovery*, Phys. Rev. A **83**, 012707 (2011).

47. S. J. Wickramarachchi, B. S. Dassanayake, D. Keerthisinghe, A. Ayyad and J. A. Tanis, *Electron transmission through a microsize tapered glass capillary*, Nucl. Instr. and Meth. Phys. Res. B **269**, 1248 (2011).

48. B. S. Dassanayake, Ph. D. Dissertation, *Electron transmission characteristics and the production of narrow beams using glass optics*, WMU, Kalamazoo, (2011).

49. N. Gao, I. Ponomarev, Q. F. Xiao, W. M. Gibson and D. A. Carpenter, *Enhancement of microbeam x-ray fluorescence analysis using monolithic polycapillary focusing optics*, App. Phys. Lett. **71**, 23 (1997).

50. T. Nebiki, M. H. Kabir and T. Narusawa, *In-air PIXE analysis by means of glass capillary optics*, Nucl. Inst. and Meth. Phys. Res. B **249**, 226(2006).

51. T. Nebiki, D. Sekiba, H. Yonemura, M. Wild, S. Ogura, H. Yamashita, M. Matsumoto, K. Fukutani, T. Okano, J. Kasagi, Y. Iwamura, T. Itoh, S. Kuribayashi, H. Matsuzaki and T. Narusawa, *Taper angle dependence of the focusing effect of high energy heavy ion beams by glass capillaries,* Nucl. Inst. and Meth. Phys. Res. B **266** 1324-1327 (2008).

52 G. Kowarik, R. J. Bereczky, F. Aumayer and K. Tokesi. *Production of microbeam of slow highly charged ions with a single microscopic glass capillary*. Nucl. Inst. and Meth. Phys. Res. B **267**, 2277 (2009).

53 A. Ayyad, B. S. Dassanayake, A. Kayani and J. A. Tanis, *Transmission of fast highly charged ions through a single glass macrocapillary,* AIP Conf. Proceedings **1336,**91 (2011).

54 Z. Gong, S. Yan, H. Ma, R. Nie, J. Xue and Y. Wang. *Study of tapered glass capillary focusing MeV ion beam*. Nucl. Inst. and Meth. Phys. Res. B **272** 370-373 (2012).

55 A. Ayyad, B. S. Dassanayake, D. Keerthisinghe, T. Ikeda, A. Kayani and J. A. Tanis, *Transmission of fast highly charged ions through single and tapered glass capillaries*, Phys. Scr. T **156**, 014058 (2013).

56 J. Yokoe, H. Tsuchida, K. Nishimura, R. Murakosi, S. Mori, M. Naitoh, T. Majima and A. Itoh, *Charge-state distributions of fast diatomic carbon ions and dissociated fragments passing through microcapillaries*, J. Phys. B. At. Mol. Opt. Phys. **46**, 115201 (2013).

57 J. Hasegawa, S. Jaiyen, C. Polee, N. Chankow and Y. Oguri. *Transport mechanism of MeV protons in tapered glass capillaries*, Jour. of App. Phy. **110**, 044913 (2011).

58 S. Jaiyen, N. Chankow, J. Hasegawa and Y. Oguri, *Effect of wall material and shape on MeV focusing ability of tapered capillary optics*, Nucl. Inst. and Meth. Phys. Res. B **271**, 13 (2012).

59 T. Ikeda , Y. Kanai, Y. Iwai, T. M. Kojima, K. Maeshima, W. Meissl, T. Kobayashi, T. Nebiki, S. Miyamoto, G. P. Pokhil, T. Narusawa, N. Imamoto and Y. Yamazaki, *Glass capillary optics for producing nanometer sized beams and its applications*, Surface and Coating Tech. **206**, 859 (2011).

60 T. M. Kojima, D. Tomono, T. Ikeda, K. Ishida, Y. Iwai, M. Iwasaki, Y. Matusuda, T. Matusuzaki and Y. Yamazaki, *Density enhancement of Muon beams with tapered glass tubes*, J. Phys. Soc. of Japan **76**, 093501, (2007).

61 M. Kato, W. Meissl, K. Umezawa, T. Ikeda and Y. Yamazaki, *Real-time observation of Escherichia coli cells under irradiation with a 2-MeV* H^+ *microbeam*, App. Phys. Lett. **100**, 193702 (2012).

62 D. Sekiba, H. Yonemura, T. Nebiki, M. Wilde, S. Ogura, H. Yamashita, M. Matsumoto, J. Kasagi, Y. Iwamura, T. Itoh, H. Matsuzaki, T. Narusawa and K. Fukutani, *Development of micro-beam NRA for 3D-mapping of hydrogen distribution in solids: Application of tapered glass capillary to 6 MeV* ^{15}N *ion*, Nucl. Inst. and Meth. Phys. Res. B **266**, 4027 (2008). D. Sekiba, H. Yonemura , S.

Ogura, M. Matsumoto, Y. Kitaoka and Y. Yokoyama, *Dvelopment of micro-beam NRA for hydrogen mapping: Observation of fatigue-fractured surface of glassy alloys,* Nucl. Inst. and Meth. Phys. Res. B **269**, 627 (2011).

63 A. S. Schlachter, J. W. Stearns, W. G. Graham, K. H. Berkner, R. V. Pyle, and J. A. Tanis, *Electron capture for fast highly charged ions in gas targets: An empirical scaling rule*, Phys. Rev. A **27**,3372 (1983).

64 W. G. Graham, K. H. Berkner, E. M. Bernstein, M. Clark, R. H. McFarland, T. J. Morgan, A. S. Schlachter, J. W. Steams, M. P. Stockli and J. A. Tanis, *Charge-state dependence of single-electron-capture and –loss cross sections for highly stripped V ions in He at 8.55 MeV amu*$^{-1}$, J. Phys. B: At. Mol. Phys. 18 2503 (1985).